JGR Oceans

RESEARCH ARTICLE
10.1029/2018JC014683

Evolution of the Seasonal Surface Mixed Layer of the Ross Sea, Antarctica, Observed With Autonomous Profiling Floats

David F. Porter[1], Scott R. Springer[2], Laurie Padman[3], Helen A. Fricker[4], Kirsty J. Tinto[1], Stephen C. Riser[5], Robin E. Bell[1], and the ROSETTA-Ice Team

[1]Lamont-Doherty Earth Observatory, Columbia University, New York, NY, USA, [2]Earth & Space Research, Seattle, WA, USA, [3]Earth & Space Research, Corvallis, OR, USA, [4]Scripps Institution of Oceanography, La Jolla, CA, USA, [5]School of Oceanography, University of Washington, Seattle, WA, USA

Key Points:
- First aircraft deployments of profiling floats near an ice shelf front document heat and freshwater evolution in spring and summer
- Multiyear time series of Ross Sea upper-ocean hydrography under sea ice reveal annual cycle and interannual variability
- Summer upper-ocean freshwater budgets require substantial lateral fluxes of ice melt from the Amundsen Sea, and from the Ross Ice Shelf

Supporting Information:
- Supporting Information S1

Correspondence to:
D. F. Porter,
dporter@ldeo.columbia.edu

Citation:
Porter, D. F., Springer, S. R., Padman, L., Fricker, H. A., Tinto, K. J., Riser, S. C., et al. (2019). Evolution of the seasonal surface mixed layer of the Ross Sea, Antarctica, observed with autonomous profiling floats. *Journal of Geophysical Research: Oceans*, *124*, 4934–4953. https://doi.org/10.1029/2018JC014683

Received 15 OCT 2018
Accepted 29 JUN 2019
Accepted article online 5 JUL 2019
Published online 18 JUL 2019

Abstract Oceanographic conditions on the continental shelf of the Ross Sea, Antarctica, affect sea ice production, Antarctic Bottom Water formation, mass loss from the Ross Ice Shelf, and ecosystems. Since ship access to the Ross Sea is restricted by sea ice in winter, most upper ocean measurements have been acquired in summer. We report the first multiyear time series of temperature and salinity throughout the water column, obtained with autonomous profiling floats. Seven Apex floats were deployed in 2013 on the midcontinental shelf, and six Air-Launched Autonomous Micro Observer floats were deployed in late 2016, mostly near the ice shelf front. Between profiles, most floats were parked on the seabed to minimize lateral motion. Surface mixed layer temperatures, salinities, and depths, in winter were −1.8 °C, 34.34, and 250–500 m, respectively. Freshwater from sea ice melt in early December formed a shallow (20 m) surface mixed layer, which deepened to 50–80 m and usually warmed to above −0.5 °C by late January. Upper-ocean freshening continued throughout the summer, especially in the eastern Ross Sea and along the ice shelf front. This freshening requires substantial lateral advection that is dominated by inflow from melting of sea ice and ice shelves in the Amundsen Sea and by inputs from the Ross Ice Shelf. Changes in upper-ocean freshwater and heat content along the ice shelf front in summer affect cross-ice front advection, ice shelf melting, and calving processes that determine the rate of mass loss from the grounded Antarctic Ice Sheet in this sector.

Plain Language Summary Measurements of temperature and salinity in coastal Antarctic waters are generally restricted to summer when sea ice disappears so that ships can operate there. Moored sensors can collect data through winter but are usually deployed below 200–300 m to minimize risk of damage from drifting icebergs. We describe a novel approach, using autonomous profilers deployed by ship and aircraft, to collect data from the seabed to the ocean surface throughout the year. We deployed 13 profilers in the Ross Sea, Antarctica. Most profilers were programmed to sit on the seabed between profiles to minimize drift and to continue profiling even when ice cover prevented their ascent to the surface. As expected, annual changes in upper-ocean temperature and salinity were closely related to seasonal changes in sea ice. However, the upper ocean continued to freshen even after the sea ice had all melted, suggesting that substantial amounts of freshwater must be coming from ice melting in the adjacent Amundsen Sea. Increasing our understanding of sources of freshwater in the Ross Sea will improve our predictions of this region's changing role in Antarctic sea ice formation, ice loss from the Antarctic Ice Sheet, and Southern Ocean ecosystems.

1. Introduction

The Ross Sea (Figure 1) is a major region of sea ice formation (Comiso et al., 2011) and water mass transformation (Orsi et al., 1999) and is the most biologically productive area of the Southern Ocean (Arrigo et al., 1998); its ecological significance (Smith, Ainley, et al., 2012) is highlighted by recent designation of the Ross Sea Marine Protected Area (CAMLR, 2016). The distribution and properties of water masses in this region (Orsi & Wiederwohl, 2009) represent the combined response to advection onto and off the continental shelf and ocean interactions with the atmosphere, sea ice and ice shelf, summarized by Smith, Sedwick, et al. (2012). Thermohaline circulation extends under the Ross Ice Shelf, which covers an area of ~480,000 km^2 in the southern Ross Sea. Advection of ocean heat under the ice shelf results in basal

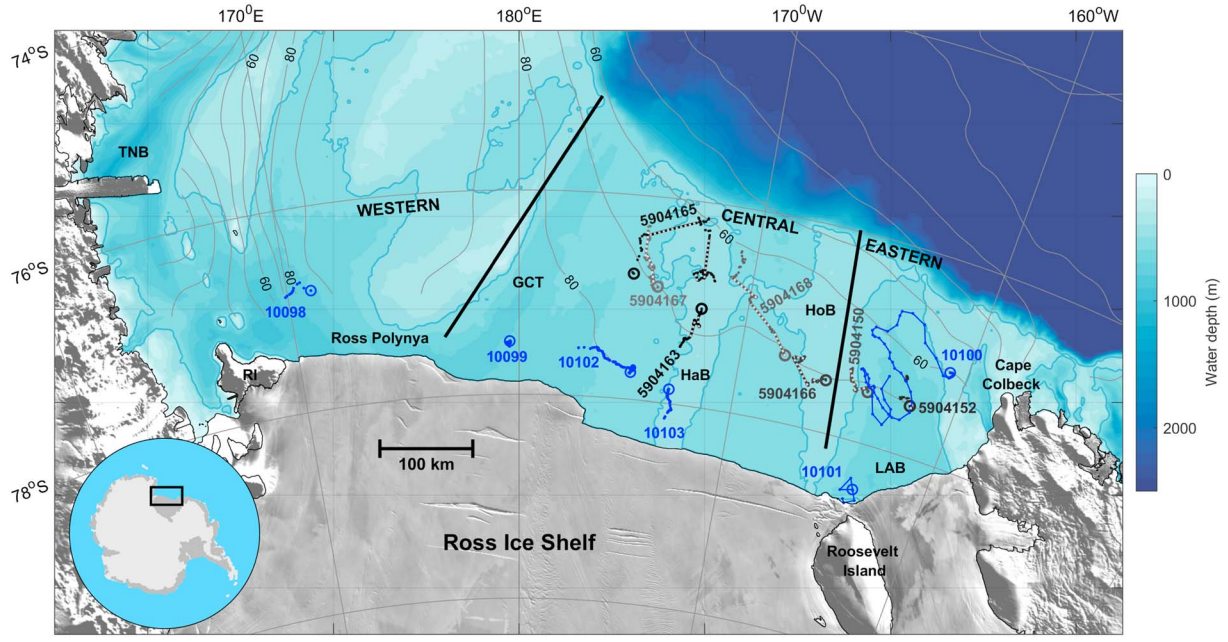

Figure 1. Location map of the Ross Sea continental shelf showing the trajectories of the 13 floats used in this study. Seven Apex floats deployed in 2013 are marked in black/gray; dotted line segments connect their last known position in a season with the first known position the following season. Six ALAMO floats deployed in late 2016 are marked by circles with labeled blue dotted trajectories. LAB = Little America Basin; HaB = Hayes Bank; HoB = Houtz Bank; GCT = Glomar Challenger Trough; TNB = Terra Nova Bay. Bathymetry is from RTOPO2 (Schaffer et al., 2016), with 500-m isobath highlighted in blue. Background is from the MODIS Mosaic of Antarctica (Scambos et al., 2007). Gray contours over open water are mean annual sea ice-free days (concentration <25%) from Special Sensor Microwave Imager. The western, central, and eastern regions are separated by the bold black lines.

melting, which constitutes 25–30% of the mass loss from this cold-water ice shelf (Depoorter et al., 2013; Rignot et al., 2013).

Over recent decades, the Ross Sea has experienced large changes in annual-averaged sea ice production and transport (Comiso et al., 2011; Holland et al., 2017), the properties of deep water masses (Budillon et al., 2011; Jacobs & Giulivi, 2010), and Antarctic Bottom Water outflows (Gordon et al., 2015). These changes in annual averages depend on processes that vary on seasonal timescales forced by the annual cycle of atmospheric state, including fluxes of heat, freshwater, and momentum. For example, production of dense High Salinity Shelf Water (HSSW) in the Ross Shelf and Terra Nova Bay polynyas occurs entirely in winter (Dale et al., 2017; Jacobs & Comiso, 1989; Rusciano et al., 2013). The seasonality of both HSSW production and circulation of Ice Shelf Water (ISW) from under the Ross Ice Shelf contributes to seasonal variability of Antarctic Bottom Water production near the continental shelf break (Budillon et al., 2011). Local warming of the upper ocean near the Ross Ice Shelf front, which contributes to the observed rapid melting in the ice shelf's frontal zone (Arzeno et al., 2014; Horgan et al., 2011; Malyarenko et al., 2019; Moholdt et al., 2014; Stewart et al., 2019; Tinto et al., 2019), only occurs during austral summer when there is minimal sea ice. The southward flux and hydrographic properties of the subsurface layer of modified Circumpolar Deep Water (mCDW) near Hayes Bank also vary seasonally (Pillsbury & Jacobs, 1985). Quantifying these processes on seasonal timescales requires acquiring data through at least a full annual cycle.

Upper-ocean hydrography in the Ross Sea has been extensively sampled by Conductivity-Temperature-Depth (CTD) profiling from ships; see Orsi and Wiederwohl (2009), their Figure 1. However, these data are biased toward the austral summer when low sea ice concentration allows ship access. Two hydrographic sections made across the west-central Ross Sea in October–November 1996 and April 1997 (Gordon et al., 2000) provide some guidance on ocean state preceding and following the open water period but do not provide data through winter. Furthermore, ship-based CTD surveys do not provide time series of variability that are needed to identify specific processes driving the observed hydrographic changes. Moored sensors, such as those reported by Pillsbury and Jacobs (1985), Whitworth and Orsi (2006), and Budillon et al. (2011), provide time series throughout the mooring deployment period, which is usually more than 1 year; however,

moored sensors have typically been deployed below 200- to 300-m depth to avoid possible damage by drifting icebergs. These temporal and depth restrictions on data availability lead to aliasing in annual mean gridded hydrographic products such as the World Ocean Atlas (Locarnini et al., 2013) and the Orsi and Wiederwohl (2009) data set for the Ross Sea. The resulting biases complicate assessment of climate model performance (e.g., Little & Urban, 2016), the use of these fields as drivers for ice sheet models (e.g., DeConto & Pollard, 2016; Joughin et al., 2014), and the accuracy of long-term hydrographic trends (Schmidtko et al., 2014).

Some progress has recently been made in extending upper-ocean measurements into the nonsummer periods. Deployments of CTD satellite relay data loggers (CTD-SRDLs) on seals (e.g., Charrassin et al., 2008; Padman et al., 2012; Roquet et al., 2013) have provided data from under sea ice in some regions since 2004. Piñones et al. (2019) used CTD-SRDL data collected in 2010-2012 in the southwest Ross Sea to describe the spatially-averaged seasonal cycle of upper ocean hydrography near Ross Island. However, these sensors are of much lower accuracy than those on ship CTD systems, and the sampling distribution is determined by the seals' foraging behavior. Ice-tethered profilers, routinely used in the Arctic (e.g., Cole et al., 2014), have been deployed for short periods in the Antarctic (Ackley et al., 2015) but cannot sample a complete annual cycle because sea ice disappears from most regions each summer, either by melting or advection. A more promising approach to obtaining high-quality upper-ocean hydrographic data continuously for long periods involves the use of autonomous profiling floats, such as the Apex floats used in the Argo program (Riser et al., 2016; Roemmich et al., 2009). Apex floats can make repetitive dives from the surface to 2,000 m and can be programmed to continue to profile while avoiding contact with sea ice (Klatt et al., 2007; Silvano et al., 2019; Wong & Riser, 2011). Pellichero et al. (2017) combined vessel CTD profiles (1906–2012), Argo float data (2002–2014), and CTD-SRDL data from marine mammals (2004–2014) to map seasonal variability of the Southern Ocean mixed layer. However, the lack of well-resolved time series limits the use of these data for assessing specific processes such as intermittent advection and response to large atmospheric forcing events.

Here, we report new observations of the temporal variability of hydrography over the southern Ross Sea continental shelf (Figure 1) from the seabed to the ocean surface during the period December 2013 to March 2017, obtained with profiling floats deployed by ship and aircraft (section 2). We use these data to describe the seasonal and interannual variability of upper-ocean hydrography of the southern Ross Sea (section 3) and estimate the heat and freshwater exchanges between the ocean, atmosphere, sea ice, and ice shelf, focusing on the transition from late winter to summer and into early autumn (section 4). These measurements and analyses provide insights into the processes that will determine future changes in the Ross Sea and Ross Ice Shelf and ice loss from the adjacent grounded portions of the Antarctic Ice Sheet (Tinto et al., 2019).

2. Data and Methods

2.1. Autonomous Profiling Floats

Two independent sets of autonomous profiling floats acquired data over a broad region of the continental shelf in the Ross Sea (Figure 1 and supporting information Table S1). In December 2013, eight Apex floats were deployed from the U. S. icebreaker *Nathaniel B. Palmer*, cruise NPB-1310, along a line roughly 100–150 km north of the Ross Ice Shelf front. One Apex float failed during the first summer and was not used in this study; the other seven floats were still operating in March 2017, the last data used in this study (see below). In total, 1,156 Apex profiles were obtained by these seven floats during these ~3.25 years. In 2016, we air-launched six Air-Launched Autonomous Micro Observer (ALAMO) A1-XB profilers from a New York Air National Guard LC-130 aircraft operating from McMurdo Station on Ross Island, as part of the ROSETTA-Ice project (Tinto et al., 2019). One float was deployed on 30 November 2016 into open water near Ross Island. On 8–9 December 2016, five more floats were deployed, four into regions of open water and one into a lead in the sea ice. One of these floats was launched ~60 km west of Cape Colbeck, while the other four were launched 35–65 km from the Ross Ice Shelf front. The six ALAMO floats made a total of 231 dives. Three ALAMO floats survived the summer season, last reporting as sea ice began to grow in early March 2017.

All floats carried SeaBird SBE41 sensors to measure conductivity (C), temperature (T), and pressure (P). Profiles of practical salinity (S_P), potential temperature (θ), potential density (σ_θ), and depth (z) were derived from these measurements (Argo, 2000). The time interval between vertical profiles for the Apex floats was nominally 7 days, and data were averaged to 2-decibar (dbar) intervals. Five of the six ALAMO floats

Table 1
List of All Floats Used in This Study; Seven Apex Floats (2013–2017) and Six ALAMO Floats (2016–2017)

		2013/2014		2014/2015		2015/2016		2016/2017	
Float	Region	First	Last	First	Last	First	Last	First	Last
Apex									
5904152	Eastern	21 Dec[a]	14 Feb	27 Nov	11 Mar	19 Dec	19 Feb	18 Dec	25 Feb
5904150	Eastern	21 Dec[a]	28 Feb	28 Dec	07 Mar	21 Dec	29 Feb	19 Dec	12 Mar
5904166	Central	21 Dec[a]	28 Feb	03 Jan	07 Mar	21 Dec	28 Feb	12 Dec	13 Mar
5904168	Central	21 Dec[a]	28 Feb	10 Jan	07 Mar	21 Dec	28 Feb	13 Dec	13 Mar
5904163	Central	21 Dec[a]	07 Jan	11 Jan	08 Mar	22 Dec	29 Feb	06 Dec	13 Mar
5904167	Central	21 Dec[a]	15 Jan	18 Jan	07 Mar	22 Dec	22 Feb	21 Nov	20 Mar
5904165	Central	21 Dec[a]	21 Jan	07 Jan	03 Mar	25 Dec	26 Feb	27 Nov	19 Mar
ALAMO									
10098	Western							30 Nov[a]	12 Dec
10099	Central							13 Dec[a]	27 Feb
10100[b]	Eastern							10 Dec[a]	06 Mar
10101[c]	Eastern							10 Dec[a]	19 Dec
10102	Central							10 Dec[a]	05 Mar
10103	Central							10 Dec[a]	14 Jan[d]

Note. Regions are defined in Figure 1. Parking depths were deeper than the seabed except where indicated. Dates of first and last communications in summer sea ice free periods are given. ALAMO = Air-Launched Autonomous Micro Observer.
[a]Date of first profile. [b]ALAMO 10100 was reprogrammed to park at 300 dbar on 19 December 2017. [c]ALAMO 10101 was parked at 150 dbar. [d]Communications ceased for unknown reason.

profiled near daily, while ALAMO 10099 profiled every 4 days. The vertical sampling interval for the ALAMO floats was initially set to 10- and 50-dbar spacing above and below 250 dbar, respectively. After confirming standard operation and sufficient bandwidth for data transfers, the floats were reprogrammed to sample at 2-dbar intervals from the seabed to the surface. During parking intervals, C, T, and P were recorded every 60 and 15 min for Apex and ALAMO floats, respectively.

When a float surfaced, its position, engineering, and hydrographic data were telemetered via the Iridium satellite network. If a float were to attempt to surface when sea ice was present, the sensors and antennas would likely be damaged. To reduce this risk, each float implemented "sea ice avoidance" logic (Klatt et al., 2007; Wong & Riser, 2011) to predict the presence of sea ice from T and S_p properties measured during ascent within the depth range of 20–40 m. If specified criteria were met, the float halted its ascent, descended to its parking depth, and retried the profile plan after 1 to 10 days. The float stored data to transmit during the next successful surfacing (Table 1). We used linear interpolation to estimate positions for profiles that were acquired while under sea ice (Figure 1).

In the conventional mode of operation, autonomous floats are programmed to drift near a preselected pressure when not profiling; most floats in the deep-ocean Argo network are "parked" near 2,000 dbar (Riser et al., 2016). The average displacement between telemetered positions then provides an estimate of mean velocity at the parking depth. Only two of our floats operated in this mode. On 19 December 2016, ALAMO 10100 was reprogrammed to a parking depth of 300 dbar in water deeper than 500 m. This float then drifted along a serpentine path at rates of up to 20 km/day within the Little America Basin in the eastern Ross Sea (Figures 1 and S1). The short-lived ALAMO 10101 (Table 1), deployed in the Bay of Whales, experienced similar daily displacements at its parking depth of ~150 dbar. For all other floats, the parking depth was set to be greater than the deepest expected seabed depth in the deployment region, ensuring that the float was sitting on the seabed while not actively profiling. For this "bottom-parking" mode of operation, we assumed that floats do not move laterally while on the seabed. This assumption is supported by time series of pressure during bottom parking, where the records are consistent with tidal variations in sea surface height but do not contain the nontidal variability that would be expected if the floats were moving across a sloping or rough seabed. Therefore, we attributed all displacements between consecutive surface position fixes to drift during the combined 3-5 hr that the profiler was off the seabed. This time includes communicating at the surface (~1 hr), descending to the seabed (~1 hr), and the following upward profiling (~1–2 hr) after the bottom-parking period.

In March 2017, the seven Apex floats were reprogrammed to drift with the ocean circulation. Since this meant that they could then drift long distances beneath the ice without providing position information, we did not use data after this date.

The interprofile displacements (Δx) for bottom-parked floats ranged from a few hundred meters to a few kilometers (Figure S1), compared with typical values of Δx of several kilometers for free drifting ALAMOs. Since the floats ascend and descend at a nearly uniform rate, horizontal displacements for bottom-parked floats can be interpreted as estimates of depth-averaged velocity for the time periods while the float is off the seabed between consecutive surface positions. The distribution of depth-averaged water speeds (about 0–0.2 m/s; Figure S1**)** estimated in this manner for bottom-parked ALAMO floats was generally consistent with speeds for the free drifting ALAMOs and measurements by current meters on moorings on and near Hayes Bank close to the ice shelf front (Pillsbury & Jacobs, 1985).

During its free drifting phase, ALAMO 10100 passed close to the bottom-parked Apex 5904152 in late January 2017 (about 3 years after Apex deployments), allowing for a direct comparison of their measurements. Two approximately concurrent and collocated profile pairs indicate good agreement between the temperature and salinity recorded by the floats (Figure S2). The largest differences were in the surface mixed layer (SML), where interfloat differences in both T and S_P were comparable to the daily variability measured by ALAMO 10100. The thin, warm layer near 150–200 m, just below the upper pycnocline, was slightly warmer in both ALAMO profiles than in the Apex. ALAMO 10100 observed a 50-m-thick warm and salty layer near 400 m, whereas Apex T and S_P profiles were nearly uniform through that depth range. Below this layer, from ~480 m down to the seafloor, the mean differences between the nearest Apex and ALAMO T and S_P profiles were less than 0.0014 °C and 0.0022, respectively. These small differences give us confidence that the sensor drift on Apex 5904152, 3 years after deployment, was negligible. For temperature, this is supported by values of minimum upper-ocean temperatures recorded every winter during active sea ice formation.

2.2. Satellite Observations of Sea Ice Concentration

We used daily sea ice concentration, (C_{ice}), derived from Special Sensor Microwave Imager multichannel passive microwave imagery (Tschudi et al., 2016) and averaged to a polar stereographic grid in 25 × 25-km cells, to determine sea ice cover above each float. These data were processed with the NASA Team algorithm (Markus & Cavalieri, 2000).

2.3. Upper-Ocean Heat and Freshwater Budgets

Upper-ocean heat and freshwater contents (OHC in gigajoules per square meter [GJ/m^2] and OFWC in meter, respectively) are the depth-integrated ocean responses to net heat and freshwater fluxes at the surface, vertical fluxes from the underlying ocean, and horizontal advection and mixing.

2.3.1. Upper-Ocean Heat and Freshwater Content

We defined OHC as the vertically integrated heat anomaly relative to the surface freezing temperature (e.g., Martinson & McKee, 2012)

$$OHC = \int_{-H_{\mathrm{int}}}^{0} \rho_0 \, c_p \left(\theta - T_{f0}\right) \mathrm{d}z, \tag{1}$$

where H_{int} is a fixed depth in meters below sea level, ρ_0 is a constant ocean density equal to 1027.7 kg/m^3, c_p is the heat capacity of seawater (taken as a constant 3,850 J/kg/K), and T_{f0} is the surface freezing temperature of seawater with a reference salinity S_{p0} (chosen to be 34.55, the maximum surface salinity reported by any float). The time tendency, $\frac{\partial(\mathrm{OHC})}{\partial t}$, is balanced by fluxes across the top and bottom of the layer and horizontal advection

$$\frac{\partial(\mathrm{OHC})}{\partial t} = Q_{\mathrm{sfc}} - Q_{z=-H_{\mathrm{int}}} - \rho_0 c_p \int_{-H_{\mathrm{int}}}^{0} \nabla_H \cdot (\mathbf{v}\theta) \mathrm{d}z. \tag{2}$$

In equation (2), Q_{sfc} (W/m^2) is the net heat flux to the ocean from the surface (atmosphere, plus ice when present), and $Q_{z=-H_{\mathrm{int}}}$ is the vertical flux at the lower integration depth limit. This flux is the sum of vertical advection (upwelling) and diffusion. The last term in equation (2) is the vertically integrated horizontal heat

flux divergence, where **v** is the horizontal current velocity vector and ∇_H is the horizontal gradient operator, and includes advection of mean gradients by mean currents and eddy heat transports.

The vertical heat flux at the lower integration depth limit, $Q_{z=-H_{\text{int}}}$, is given by

$$Q_{z=-H_{\text{int}}} = \rho_0\, c_p \left(\theta - T_{f0}\right)_{-H_{\text{int}}} w_{Ek} + \rho_0\, c_p K_z \frac{\partial \theta}{\partial z}. \tag{3}$$

In equation (3), $w_{Ek} = \nabla \times (\boldsymbol{\tau}/\rho_0 f)$ is the Ekman upwelling rate, where f is the Coriolis parameter and $\boldsymbol{\tau}$ is the surface wind stress vector. Note that we do not include effects of a sea ice cover on the transmission of wind stress to the ocean since the focus of this paper is primarily on sea ice free periods. Kim et al. (2017) provide more information of the effects of sea ice on upwelling driven by wind stress curl. We estimated the diffusion term from vertical eddy diffusivity, K_z, which may be provided by a turbulence closure model or using typical ocean values of 10^{-6} to 10^{-4} m^2/s (see, e.g., Ledwell et al., 1993; Smith & Klinck, 2002).

Similarly, we calculate OFWC (e.g., Condron et al., 2009) as

$$OFWC = \int_{-H_{\text{int}}}^{0} \left(1 - \frac{S_p(z)}{S_{p0}}\right) \mathrm{d}z. \tag{4}$$

Changes in OFWC obey a conservation equation similar in form to equation (2).

2.3.2. Atmospheric Fluxes From the ERA-Interim Reanalysis

We obtained estimates of surface heat, freshwater, and momentum fluxes from ERA-Interim, a global atmospheric reanalysis that solves for the best fit between observations and dynamical constraints (Dee et al., 2011). Output was obtained on a 0.75° grid (~17 × 83 km near the ice shelf front) at 3-hr intervals. Ocean points in ERA-Interim may be open water or covered by some fraction of sea ice, obtained from satellite measurements of C_{ice} (section 2.2). Surface fluxes, which are calculated in the atmospheric boundary layer, are partitioned by the fraction of the surface covered by sea ice and liquid ocean surface. The net atmospheric heat flux, Q_{ATM}, is given by the sum of several components: $Q_{\text{ATM}} = Q_{\text{SW}} + Q_{\text{LW}} + Q_H + Q_E$, where Q_{SW} and Q_{LW} are the net shortwave and longwave radiative fluxes and Q_H and Q_E are the sensible and latent turbulent heat fluxes. All fluxes are defined as positive downward (i.e., heat gain by the ocean). The local atmospheric surface freshwater flux is given by $FW_{\text{ATM}} = (P - E)$, where P (positive down) and E (positive up) are precipitation and evaporation rates, respectively. Over the ocean close to the ice front, there may be an additional freshwater flux when snow that falls on the northern ice shelf is blown into the ocean by the prevailing southerly winds (Knuth et al., 2010); however, this term is not provided by ERA-Interim.

3. Results

3.1. Float Locations and Drift

Uncertainties in profile locations acquired while under sea ice arise from the linear interpolation of float drift between consecutive surface fixes (Figure 1). We reduced the impact of this uncertainty by aggregating the floats into three regions based on bathymetry and average hydrographic properties. The regions are denoted "western," "central," and "eastern" Ross Sea (see Figure 1). The western region was sampled only by ALAMO 10098, near Ross Island. The central region, defined here as east of Glomar Challenger Trough and west of Houtz Bank, was sampled by five Apex floats and three ALAMO floats. The eastern region, east of Houtz Bank to Cape Colbeck, was sampled by two Apex floats and two ALAMO floats.

Three central floats (Apex 5904166, 5904167, and 5904168) drifted generally northwestward, and three (Apex 5904163, 5904165, and ALAMO 10103) moved southward along the western flank of Hayes Bank. Near the ice shelf front, ALAMO 10102 moved steadily westward. ALAMO 10099, on the eastern edge of Glomar Challenger Trough, remained nearly stationary; however, this float only profiled every 4 days, reducing its exposure to ocean currents. The small net displacements of the eastern Ross Apex floats were northwestward (Figure 1), while ALAMO 10100 followed a complex path through Little America Basin during its period of free drift.

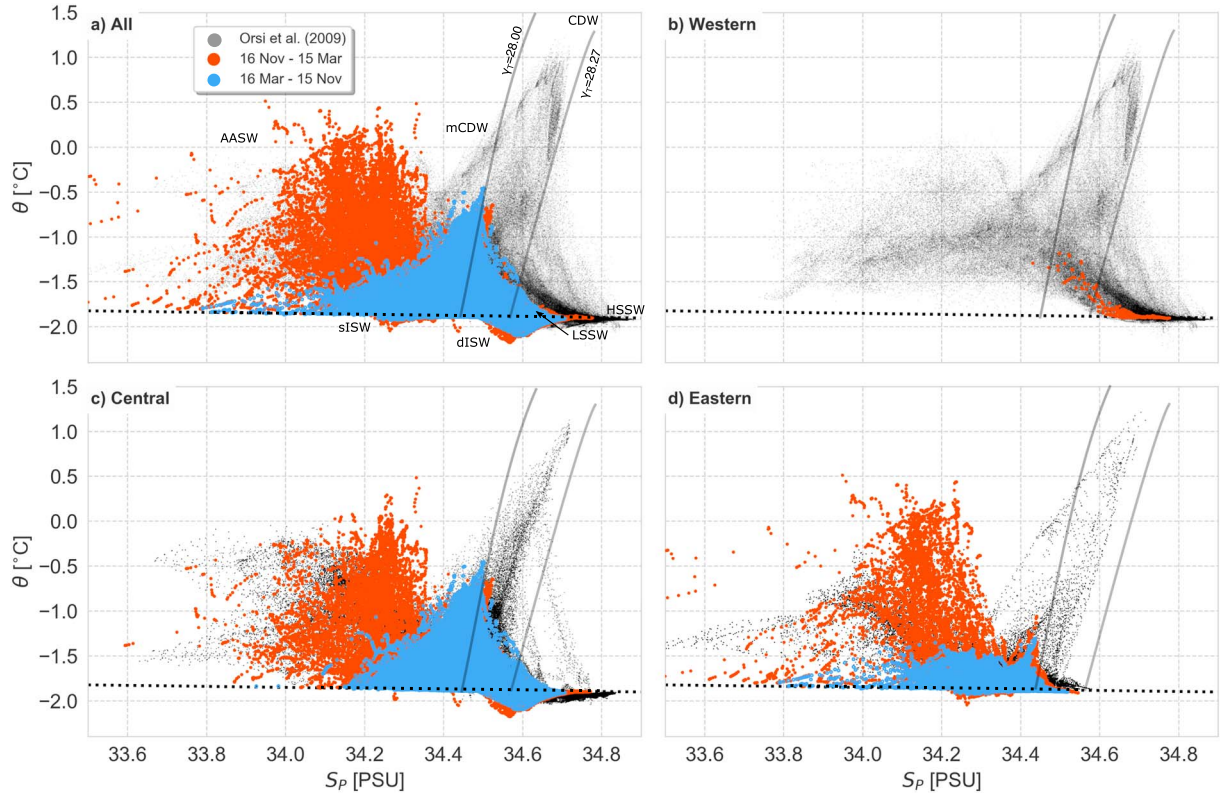

Figure 2. Ross Sea hydrography. Gray dots show distribution of potential temperature-salinity (θ-S_P) from Orsi and Wiederwohl (2009) for all their gridded 3-D fields from locations with water depth less than 800 m south of a line from Cape Colbeck to Cape Adare. Red dots are float data from austral summer (16 November to 15 March); blue dots are all other float data. Data are presented for (a) combined data from all regions and separately for (b) western, (c) central, and (d) eastern regions (see Figure 1 for region definitions). Overlain are two neutral density (γ) contours (solid black lines) used to distinguish water masses, the surface freezing point of seawater as a function of S_P (dotted line), and water mass annotations used in the text.

3.2. Overview of Hydrographic Structure

The two sets of floats sampled most of the major regional water masses that have previously been identified in the Ross Sea (Carmack, 1986); see Figure 2a. Differences in the regional distributions of water masses recorded by the floats (Figures 2b–2d) are consistent with prior studies (e.g., Orsi & Wiederwohl, 2009) including summer surveys close to the ice shelf front (e.g., Smethie & Jacobs, 2005). Examples of hydrographic profiles from the six ALAMO floats (Figure 3) demonstrate the variability of water masses by location and depth range. HSSW, with $S_P > 34.62$, was observed in both the western and central regions but not in the eastern region. Low-Salinity Shelf Water, with $S_P < 34.62$, was observed in the central and eastern regions. ISW, defined as having values of θ below the surface freezing temperature, T_{f0} (MacAyeal & Thomas, 1986), was observed close to the ice shelf front. "Deep" ISW (see Figure 3b) is formed from ice shelf melting at high pressure near the deep grounding line where HSSW comes into contact with the ice base; this water mass exits the ice shelf cavity as subsurface plumes of intermediate salinity ($34.48 < S_P < 34.68$). Some ISW is fresher ($S_P < 34.4$) and with θ closer to T_{f0} and exits the cavity as "shallow" ISW (sISW; see Nelson et al., 2017 and Robinson et al., 2010) that may directly mix into the SML close to the ice shelf front (Malyarenko et al., 2019). The sISW is formed when water masses that are less saline than HSSW melt relatively shallow ice close to the ice shelf front. Ventilation of sISW into the upper ocean north of the ice shelf front may be assisted by across-front tidal currents (Arzeno et al., 2014) and by eddies whose generation may be related to density gradients and irregularities along the ice shelf edge (Li et al., 2017).

Antarctic Surface Water (AASW) is the lightest water mass, occupying broad ranges in both θ and S_P. AASW was detected by all floats in austral summer when sea ice had mostly melted and open water prevailed (typically about mid-November to mid-March). In the western region (Figure 2b), ALAMO 10098 did not survive long enough into summer to observe significant upper-ocean warming and freshening. AASW often includes

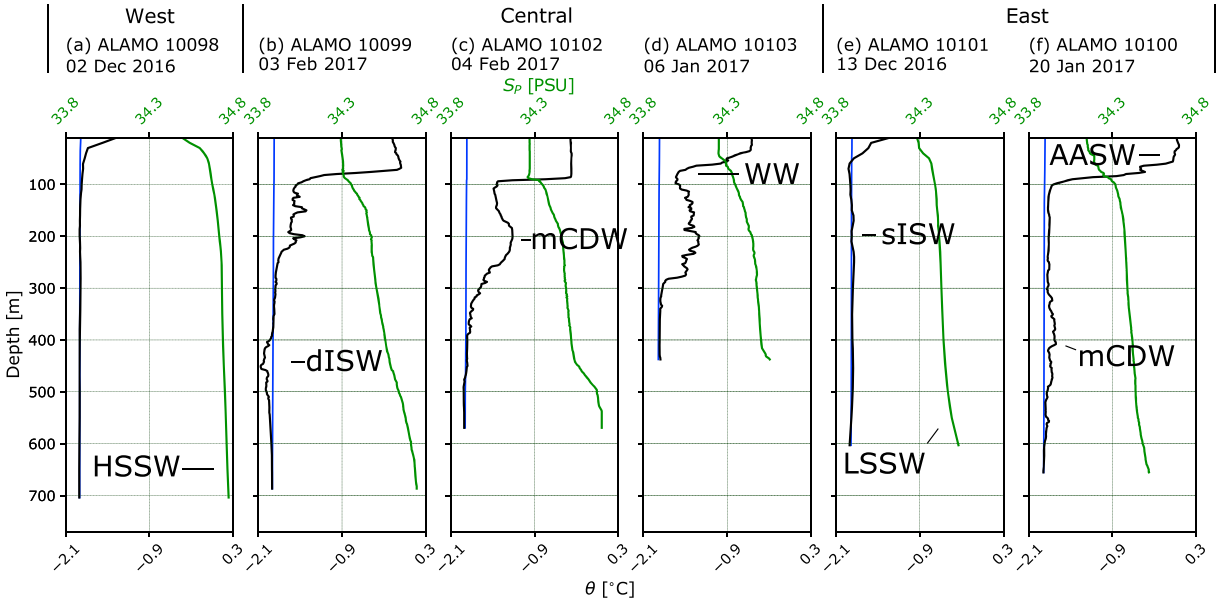

Figure 3. (a–f) Example profiles from each of the six ALAMO floats. Each panel shows potential temperature (θ: black), practical salinity (S_P: green), and the surface freezing point of seawater (T_{f0}: blue), selected to illustrate specific water masses. Panels are arranged from west to east (see Figure 1 for locations and region definitions and Table 1 for locations of floats by region). Note the date of each profile, provided above each panel. ALAMO = Air-Launched Autonomous Micro Observer; HSSW = High-Salinity Shelf Water; dISW = deep Ice Shelf Water; mCDW = modified Circumpolar Deep Water; WW = Winter Water; sISW = shallow Ice Shelf Water; LSSW = Low Salinity Shelf Water; AASW = Antarctic Surface Water.

Winter Water (Figure 3d), a cold but relatively fresh remnant of the previous winter's SML. Water masses with intermediate density include mCDW, which is formed when warm CDW located offshore of the continental shelf break mixes with shelf-resident water masses including Low Salinity Shelf Water and AASW. None of the floats analyzed here measured any pure CDW, which has not been found more than a few kilometers south of the continental shelf break (Orsi & Wiederwohl, 2009; Whitworth & Orsi, 2006).

3.3. Seasonal and Interannual Hydrographic Variability Over the Midcontinental Shelf

Upper-ocean hydrography recorded by two Apex floats (Figure 4; see supporting information Figures S3–S5 for all seven Apex floats for the full depth range) was dominated by a shallow, warm, and fresh SML in summer and a deep, cold, and saline SML in winter. Following Wong and Riser (2011), we defined the depth of the SML, H_{SML}, as the depth at which potential density was 0.05 kg/m^3 greater than at the surface. We then defined the mean potential temperature and practical salinity of the SML (θ_{SML} and $S_{P,SML}$, respectively) as averages of $\theta(z)$ and $S_P(z)$ from the surface to H_{SML}. Time series of H_{SML}, θ_{SML}, and $S_{P,SML}$ for all floats (Figure 5**)** show seasonal and interannual variability and large variations between SML characteristics in different regions.

Beginning in late November as C_{ice} decreased (Figure 5a), typical values of H_{SML} (Figure 5b) decreased rapidly from wintertime values of more than 200 m to less than 20 m by mid-December. The SML then deepened slowly during summer to 50–80 m in mid-February. Between mid-February and mid-March, sea ice growth led to further deepening of the SML. In autumn, the deepening of the mixed layer began sooner at the central floats than at the eastern floats (Figure 5b). At all locations, deepening occurred at rates between 2 and 5 m/day but ended sooner in the central Ross Sea, so that wintertime mixed layers tended to be shallower (200–300 m) in the central region than in the eastern region (300–500 m). The deepest wintertime mixed layers reached 500 m (~150 m off the seabed) at Apex 5904152 (Figure S5b).

To highlight the seasonal variability of θ_{SML} and $S_{P,SML}$, we formed composite annual cycles by averaging SML properties by week of the year over the entire observation period (>3 years). We further averaged these temporal averages across floats, with separate ensembles for the central and eastern floats. The annual cycles of mixed layer temperatures and salinities for the two ensembles followed counterclockwise loops in θ-S space (Figure 6). On 1 November, temperature was near freezing (−1.9 °C) for the eastern region and

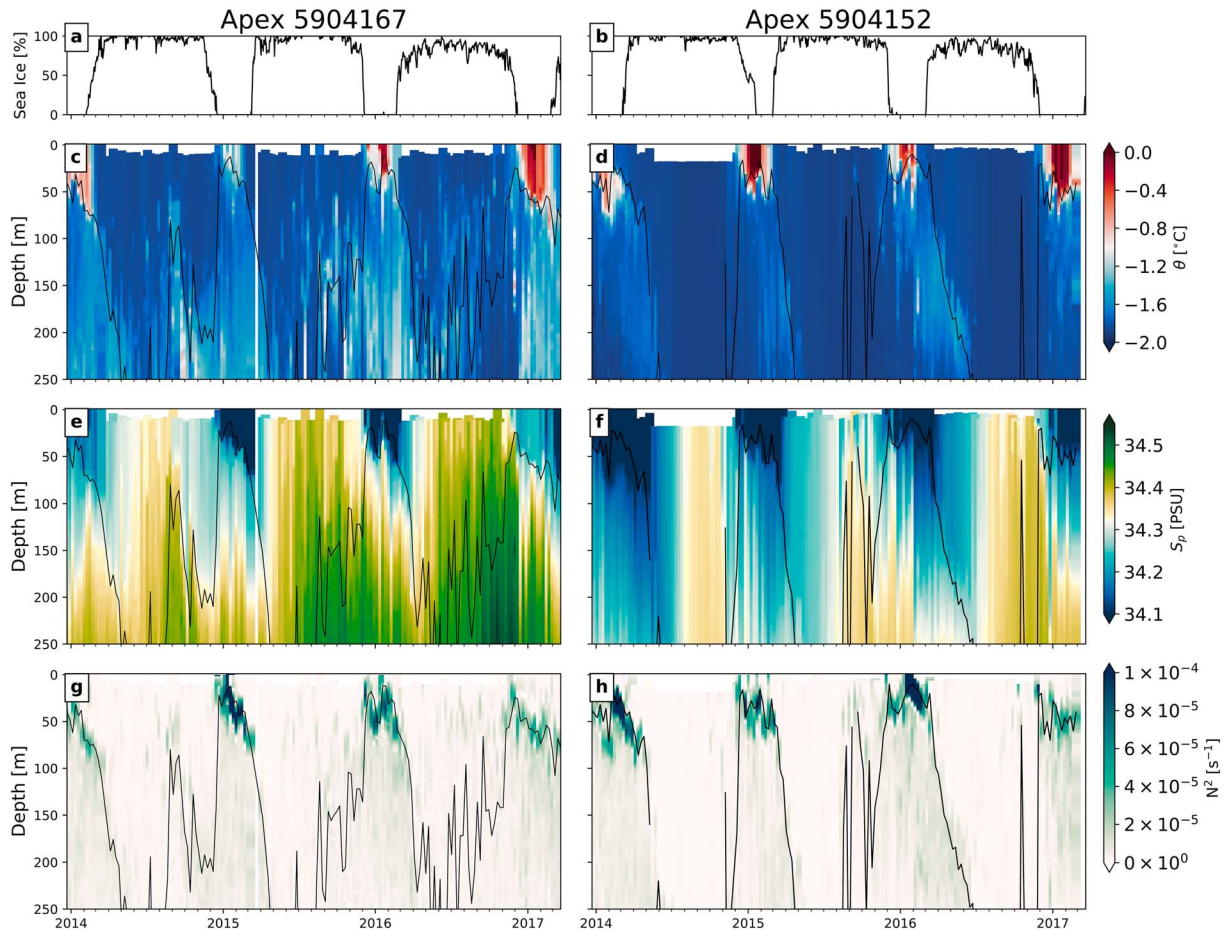

Figure 4. Sea ice concentration and upper-ocean (0–250 m) hydrographic properties for two Apex floats in the Ross Sea. Left plots are for Apex 5904167 in the central region and right plots are for Apex 5904152 in the eastern region. Rows are from top to bottom: (a, b) SSM/I sea ice concentrations, (c, d) potential temperature, (e, f) salinity, and (g, h) N^2. Black line in c–g represents H_{SML}. Missing data near the surface are due to the profilers' sea ice avoidance software (see text).

slightly warmer (about −1.8 °C) in the central region. Salinity in the SML for both regions on 1 November was 34.34. In the central region, starting from the end of winter (November) values, θ_{SML} increased and $S_{P,SML}$ decreased until February after which θ_{SML} dropped with little change in $S_{P,SML}$ until March. Values of θ_{SML} continued to drop and $S_{P,SML}$ increased through mid-March then $S_{P,SML}$ increased to return to its maximum value by November. In early winter, θ_{SML} for most floats was around −1.8 °C, slightly warmer than the corresponding surface freezing point, with θ_{SML} warming slightly (~0.1 °C) from April to October. In the eastern region, θ_{SML} and $S_{P,SML}$ were similar to the central region values until early January, but by February the mixed layer was warmer and fresher. The SML cooled but continued to freshen into early March. On 1 March, the salinity difference between the eastern and central mixed layers was greater than 0.25. In both regions, salinity increased throughout winter.

The seasonal progression of upper-ocean stratification recorded by the Apex floats was qualitatively consistent each year; however, the duration, depth, and properties of the seasonal SML varied interannually (Figures 4, 5, and S3–S5). In the eastern region, Apex floats detected warmer, more saline and deeper SMLs in summer 2014–2015 than in 2013–2014. Conversely, in the central region, the SML was cooler and fresher in 2014–2015 than in the previous summer.

3.4. Upper-Ocean Hydrographic Variability in Summer 2016–2017 Near the Ross Ice Shelf Front

Warming and freshening of the seasonal SML along the ice shelf front commenced soon after deployment of ALAMO floats (Figure 7). Typical values of H_{SML} during December and January were 40–60 m. In the latter half of the summer the SML cooled, freshened to 34.06, and deepened to 100 m by the last week of February

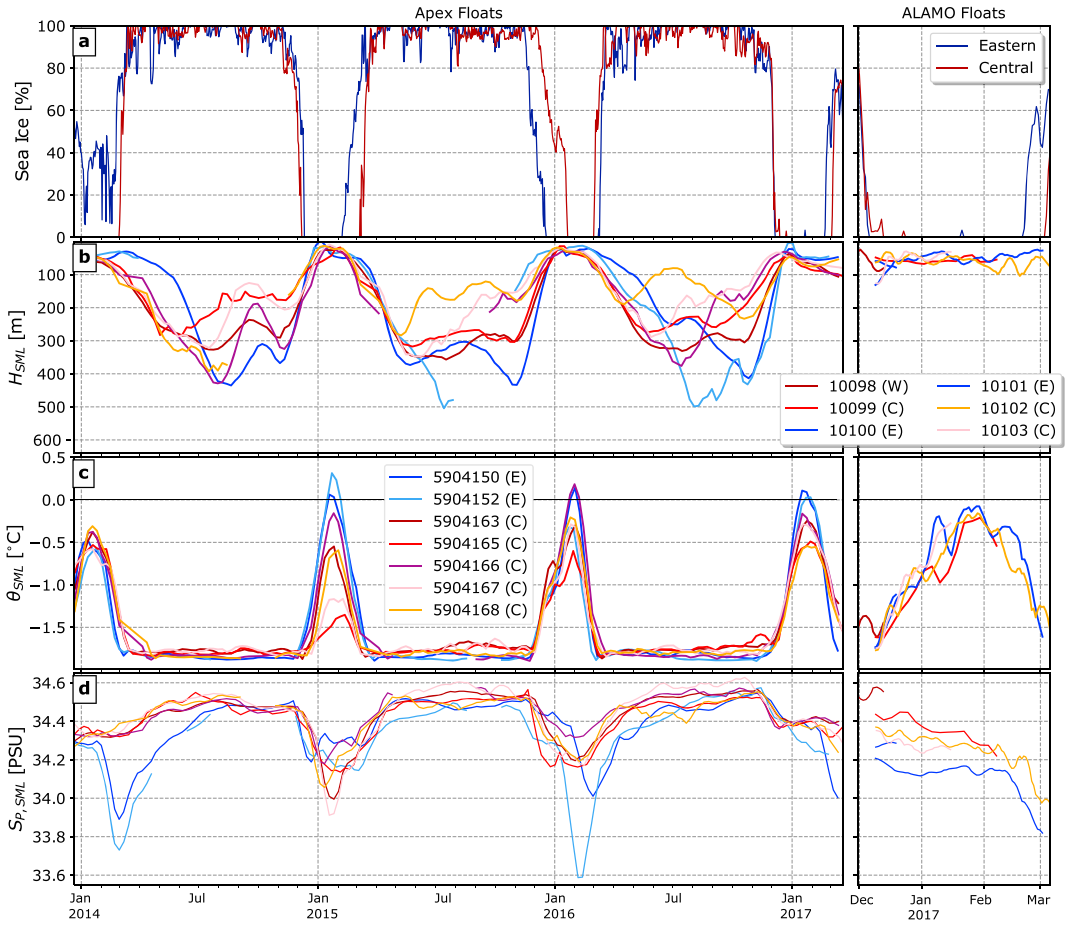

Figure 5. Sea ice concentration and properties of the surface mixed layer (SML) derived for each float. Floats in the eastern region "(E)" are in blue, central region "(C)" are in red/orange, and the western region "(W)" is in purple. Left plots are for the seven Apex floats (2014–2017); right plots are for Air-Launched Autonomous Micro Observer floats (2016–2017). Rows are from top to bottom: (a) Special Sensor Microwave Imager sea ice concentration for Apex 5904152 (eastern, blue) and 5904167 (central, red) regions. (b) SML depth, H_{SML}. (c) SML potential temperature, θ_{SML}. (d) SML salinity, $S_{P,SML}$. LOWESS smoothing at 30 and 14 days was applied to Apex and ALAMO data, respectively. ALAMO = Air-Launched Autonomous Micro Observer.

2017. For ALAMO 10102, θ_{SML} at deployment was at its minimum of −1.78 °C and $S_{P,SML}$ was ~34.38 (see, also, Figure 5) after which θ_{SML} reached a maximum of −0.03 °C on 30 January 2017. After this peak, the SML cooled while continuing to freshen, reaching a minimum salinity of 33.86 at ALAMO 10102. This variability of summer θ_{SML} and $S_{P,SML}$ near the ice shelf front was more similar to that detected by eastern Ross Sea Apex floats than to the SML variability of the nearer Apex floats in the central Ross Sea.

During the late summer period as the upper ocean cooled, near-surface density reductions due to the observed freshening exceeded the density increases due to cooling, resulting in a net decrease in near-surface density and the creation of a shallow, fresh, and cool SML overlying a near-surface temperature maximum as often seen in the Arctic (Carmack et al., 2015; Jackson et al., 2010). This feature is also seen in the Apex profiles from the midshelf region (Figures 4 and S3). In these ALAMO profiles close to the ice shelf front, this subsurface temperature maximum emerges on 12 February 2017 at 100 m (Figure 7b) and persists at depths of up to 150 m until the last profile on 5 March 2017, where its temperature was −0.8 °C.

4. Discussion

The annual cycles of SML properties recorded by the Apex floats (Figure 6) were closely related to the observed cycle of sea ice concentration (Figures 4 and 5). However, the relationship between seasonal variability of atmospheric and upper-ocean states is complicated by ice albedo and latent heat, freshwater, and

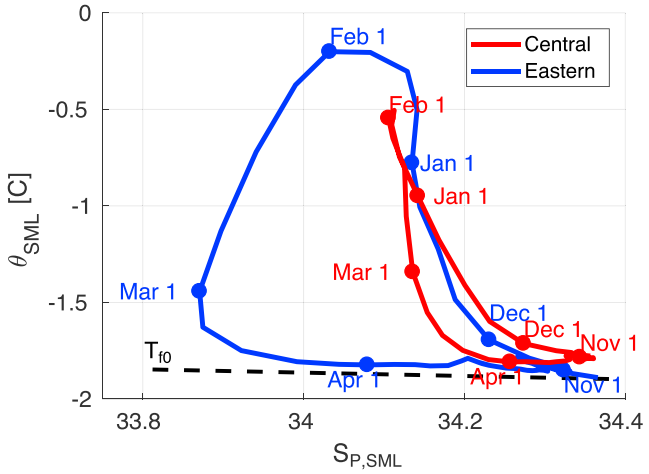

Figure 6. Composite temperature-salinity (θ_{SML}-$S_{P,SML}$) plot of surface mixed layer (SML) evolution for all Apex data. Loops are based on 3 years of data, ensemble-averaged into central (two floats) and eastern (five floats) regions. The loops are followed counterclockwise, as indicated by the dates. Dashed line indicates surface freezing temperature of seawater.

salt fluxes (Petty et al., 2013, 2014), including complex feedbacks between sea ice melting and convection (Martinson, 1990) that depend on mixing processes which are still poorly quantified. Here, we focus on the controls on upper-ocean hydrography during the summer period when C_{ice} was low, so that ocean surface heat and freshwater fluxes can be estimated from atmospheric reanalysis models without correcting for the poorly known effects of sea ice on the atmosphere-ocean fluxes. At each float location we define the summer open-water period as the time interval between the first and last successful satellite communication (Table 1).

4.1. Changes in Ocean Heat Content

We used equation (1) to calculate the ocean heat content (OHC) anomaly relative to the surface freezing temperature, $T_{f0}(S_{P0})$. We chose the integration depth, $H_{int} = 120$ m, to be deeper than the maximum summertime H_{SML} (Figure 5b) and shallower than most mCDW (Figures 3b–3d). The OHC anomaly throughout the winter was ~0.05 GJ/m^2 (Figure 8a), a small value indicating that water throughout the integration depth range was near the surface freezing temperature. Brief intervals of elevated winter OHC at two Apex floats in the central region (Figure 8a) were associated with periods of mCDW shoaling (Figures 4 and S3). OHC increased by 0.1–0.5 GJ/m^2 between winter and when maxima in OHC occurred, which was usually close to 1 February but was sometimes up to 2 weeks earlier or later. Averaged across all seven Apex floats and all 4 years, the heat gained from the date of first float communication to the time of maximum OHC corresponds to an average rate of change of 76 ± 40 W/m^2 (the quoted uncertainties in this section are one standard deviation of the 28 separate estimates). Nearly all of the seasonal heat storage in the upper 120 m was lost before the last communication of each season (Figure 8a), at an average rate of −111 ± 53 W/m^2. For summer 2016–2017, the time series of OHC from two ALAMO floats (10102 and 10099) close to the ice shelf front (Figure 8a) showed similar seasonal changes.

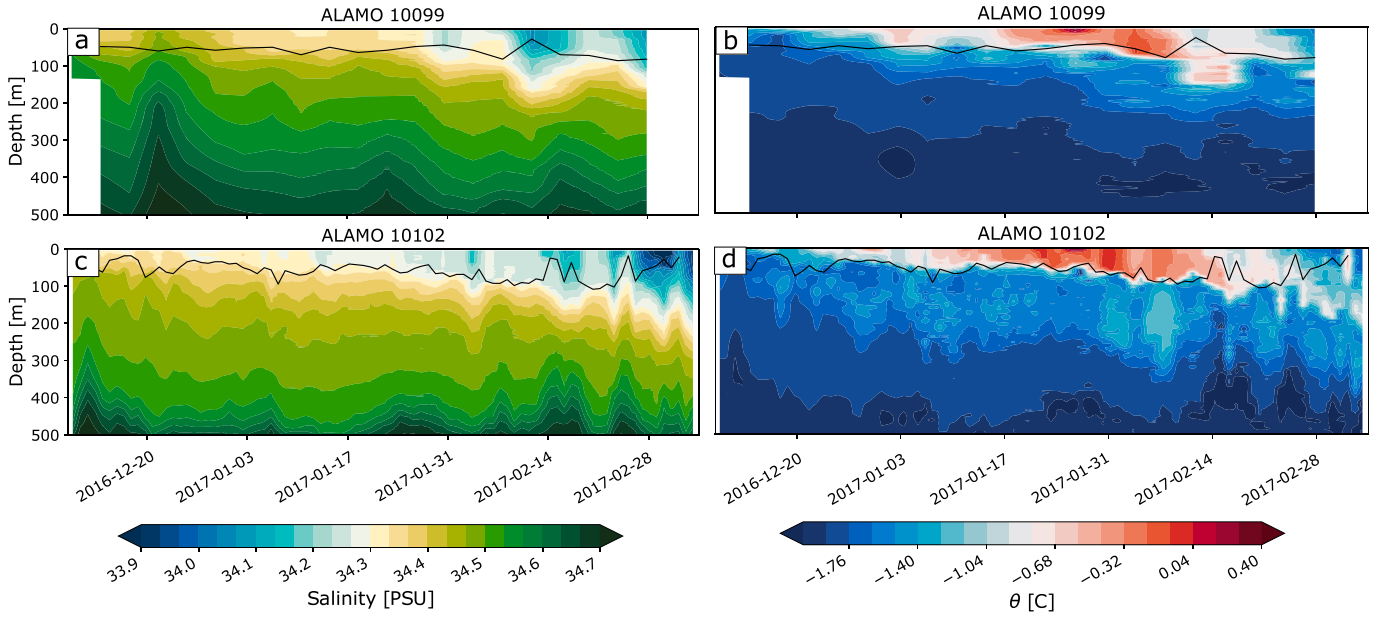

Figure 7. Hydrographic variability during summer 2016–2017 near the Ross Ice Shelf front from two ALAMO floats. (a, b) Salinity (S_P) and potential temperature (θ) for ALAMO 10099, profiling every 4 days near Glomar Challenger Trough. (c, d) S_P and θ for ALAMO 10102, profiling everyday on the western slope of Hayes Bank. Black line is the surface mixed layer depth, H_{SML}. ALAMO = Air-Launched Autonomous Micro Observer.

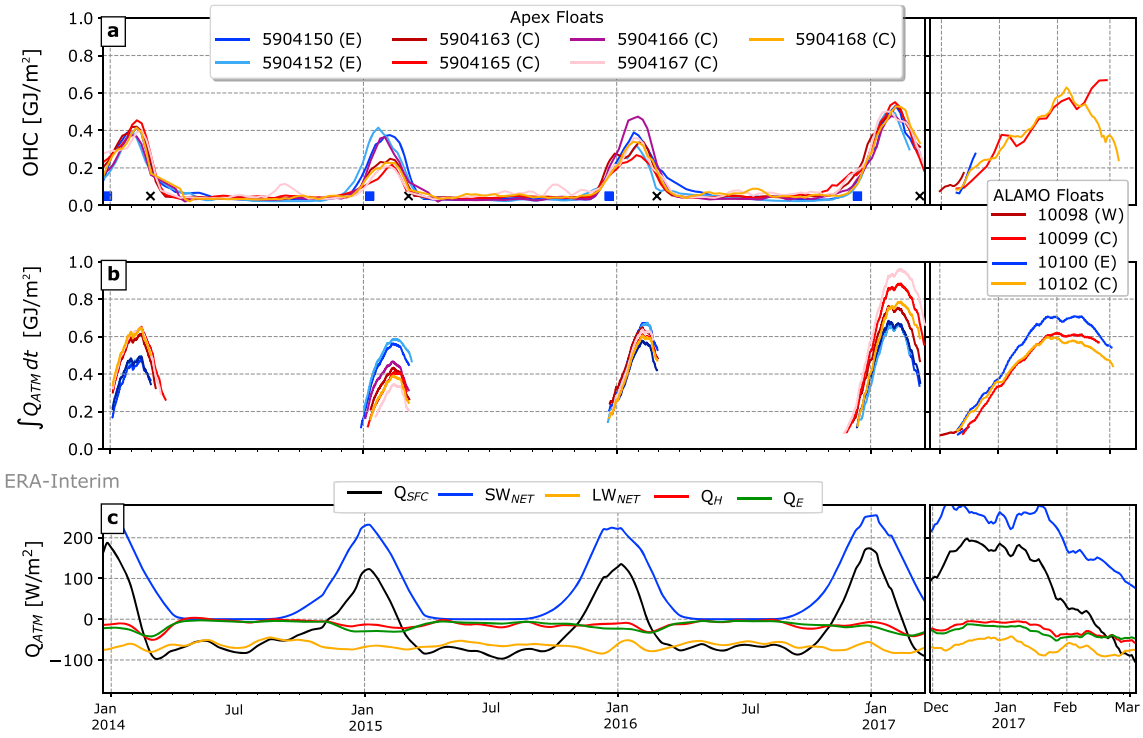

Figure 8. Measured ocean heat content compared with atmospheric forcing for each float. Floats in the eastern region (E) are in blue, central region (C) are in red/orange, and the single ALAMO float in the western region (W) is in purple. Left plots are for Apex floats (2014–2017); right plots are for ALAMO floats (2016–2017) from top to bottom: (a) Ocean heat content (OHC) in gigajoules per square meter; LOWESS smoothing was applied to Apex (30 days) and ALAMO data 14 days). Times of first and last communications of Apex 5904168 of each season are indicated by blue squares and black crosses, respectively. (b) Time-integrated ERA-Interim surface heat flux (GJ/m^2) for each float, beginning at the start of each ice-free period and ending at the time of last float communication each year. (c) Components of ERA-Interim surface heat flux from the grid cell closest to Apex float 5904163 in the central Ross Sea, with 14-day LOWESS smoothing.

During summer when C_{ice} is close to zero (Figure 5a), the surface heat flux into the ocean, Q_{SFC}, should be approximately equal to the heat flux at the base of the atmosphere, Q_{ATM}. To test how well the changes in observed OHC could be explained by local atmospheric fluxes, we integrated ERA-Interim Q_{ATM} through each summertime open-water period for each float. The integrated surface heat flux sampled at each float location increased until early February, typically 10 days later than OHC observed by the floats and then decreased through March (Figure 8b). All of the summer heat gain was due to Q_{SW}, the only positive component of surface heat flux (Figure 8c). Averaged over all floats and years, the peak magnitude of integrated heat flux exceeded the peak measured OHC by 0.18 ± 0.09 GJ/m^2. Each summer period free of sea ice ended with accumulated heat from the atmosphere exceeding the measured OHC. We used this end-of-season surplus heat to estimate that, averaged over the summer, ERA-Interim surface heat fluxes exceeded the amount needed to explain changes in observed OHC by 44 ± 18 W/m^2. This bias may represent errors in the fluxes provided by ERA-Interim or that there is a cooling contribution in summer from other sources such as melting of residual sea ice and icebergs and advection of cold water.

Interannual variability in OHC and the integrated surface flux from ERA-Interim was primarily related to year-to-year changes in the onset of sea ice loss and the duration of the summer period of minimal sea ice concentration. In summer 2014–2015, peak OHC in the eastern region was nearly double that in the central region, where the onset of open water was 2-3 weeks later than typical, based on time series of sea ice concentration (Figure 5a) and float communication records (Table 1). In agreement with Holland et al. (2017), we suggest that the lingering ice pack delayed the increase in absorbed shortwave radiation until after the insolation peak, resulting in relatively little warming (Figure 8b). Conversely, in December 2016, earlier and more extensive open water (beginning in late November in the central region) captured the seasonal peak of solar radiation and lengthened the period for heat accumulation, leading to a larger peak in OHC in summer 2016–2017. The early disappearance of sea ice in that summer was due to wind stress

anomalies that advected sea ice off the continental shelf (Turner et al., 2017, their Figure 3c). In early 2017, open water persisted into mid-March (last float communications in autumn 2017 from Table 1). We propose that this later onset of sea ice formation in 2017 was caused by the increased upper-ocean heat stored during the 2016–2017 summer. Interannual variability in OHC will also be affected by differences in cloudiness, which alters radiation fluxes at the surface, and windiness, which changes the turbulent (sensible and latent) heat fluxes (Figure 8c).

The large differences between the integrated surface heat flux and measured heat content for the floats in some summers (Figure 8) are caused by a combination of additional heat flux components and errors in surface heat fluxes obtained from ERA-Interim. Estimated vertical fluxes at 120 m (equation (3)) are small, −4 and 1–2 W/m^2 for Ekman upwelling and turbulent mixing, respectively. We expect some contribution to local heat fluxes from the Antarctic Coastal Current delivering water from the Amundsen Sea to the eastern Ross Sea; however, this flux is difficult to quantify. Analyses of output from ocean circulation models that extend well east of the Ross Sea (e.g., Nakayama et al., 2014) would improve our understanding of the potentially seasonal contribution of advective heat fluxes to OHC variability observed by our floats.

The atmospheric flux estimates provided by ERA-Interim also contain errors. The amplitude and timing of the peak in the integrated surface heat flux (Figure 8b) can be brought into closer agreement with the observed OHC (Figure 8a) by reducing the shortwave radiation flux by a quarter or by doubling the turbulent fluxes. There are few data available in this region for constraining atmospheric reanalyses, especially over the open ocean and sea ice. Errors in Q_{SW} may be associated with errors in cloudiness and surface albedo, the latter being sensitive to ocean surface roughness at the low angles of incidence for insolation. Lenaerts et al. (2017) showed that ERA-Interim shortwave fluxes around Antarctica are biased low in the spring and autumn but not in the summer, although the Ross Sea was not studied specifically. Turbulent fluxes are sensitive to wind stress (Fusco et al., 2009). In comparisons with automated weather stations located on land and ice shelves, Rodrigo et al. (2013) found that biases in wind speed can reach 10 m/s near coastal zones, and Dale et al. (2017) found that wind speeds over the Ross Shelf Polynya are underestimated by 70%, which has a significant impact on the turbulent fluxes that sustain HSSW production in winter. Cerovečki et al. (2011) found that constraining an ocean model to observed heat content suggested that there are large biases in surface heat fluxes at high latitudes of the Southern Ocean.

4.2. Changes in Freshwater Storage

We calculated upper-ocean freshwater content (OFWC) using equation (4). For each Apex float, OFWC reached a minimum in late winter, increased during spring, reached its maximum value in summer, and declined through autumn and early winter (Figure 9a). We focus on two periods of freshwater input: spring, the transition period when sea ice is melting, and summer, after C_{ice} has declined to zero.

In spring, each float detected a change in freshwater content, between the minima near 15 October (close to the time of expected maximum sea ice volume) and the first float communication of the year (Table 1). During the springs of 2015–2017, the change in OFWC was 0.34 ± 0.05 m across all floats. We estimated the thickness of sea ice (h_{ice}) at the end of winter by assuming that the observed increase in freshwater was due solely to the complete melting of local ice. The freshwater content of sea ice is $(\rho_{ice}/\rho_0)(S_{ice}/S_0\text{-}1)(h_{ice}C_{ice})$, where ρ_{ice} and ρ_0 are densities of sea ice and ocean (taken to be 917 and 1,028 kg/m^3, respectively), and S_{ice} and S_0 are salinities of the sea ice and ocean. Assuming uniform and non-time-varying values for S_{ice} = 4 (Cox & Weeks, 1974) and C_{ice} = 0.85 (Jacobs & Comiso, 1989), we found h_{ice} = 0.51 ± 0.07 m. These values are consistent with previous estimates of winter ice thickness in the Ross Sea (Kurtz & Markus, 2012; Martin et al., 2007); however, see Kurtz and Markus (2012) and Shepherd et al. (2018) for discussions of the challenges of measuring Antarctic sea ice thickness from space. Potential sources of errors in our estimate of h_{ice} in late winter include neglecting ice transport and divergence and other processes contributing to upper-ocean freshening during this period (see below). Some of the ice clearance in spring is due to wind-driven transport off the continental shelf rather than melting within the Ross Sea (e.g., Comiso et al., 2011; Holland & Kwok, 2012; Turner et al., 2017), which reduces the ocean freshening relative to a model of local ice melt.

In summer, after the end of the primary sea ice melt season as identified by the time of first float communication (Table 1), OFWC at most floats continued to increase throughout the open-water periods

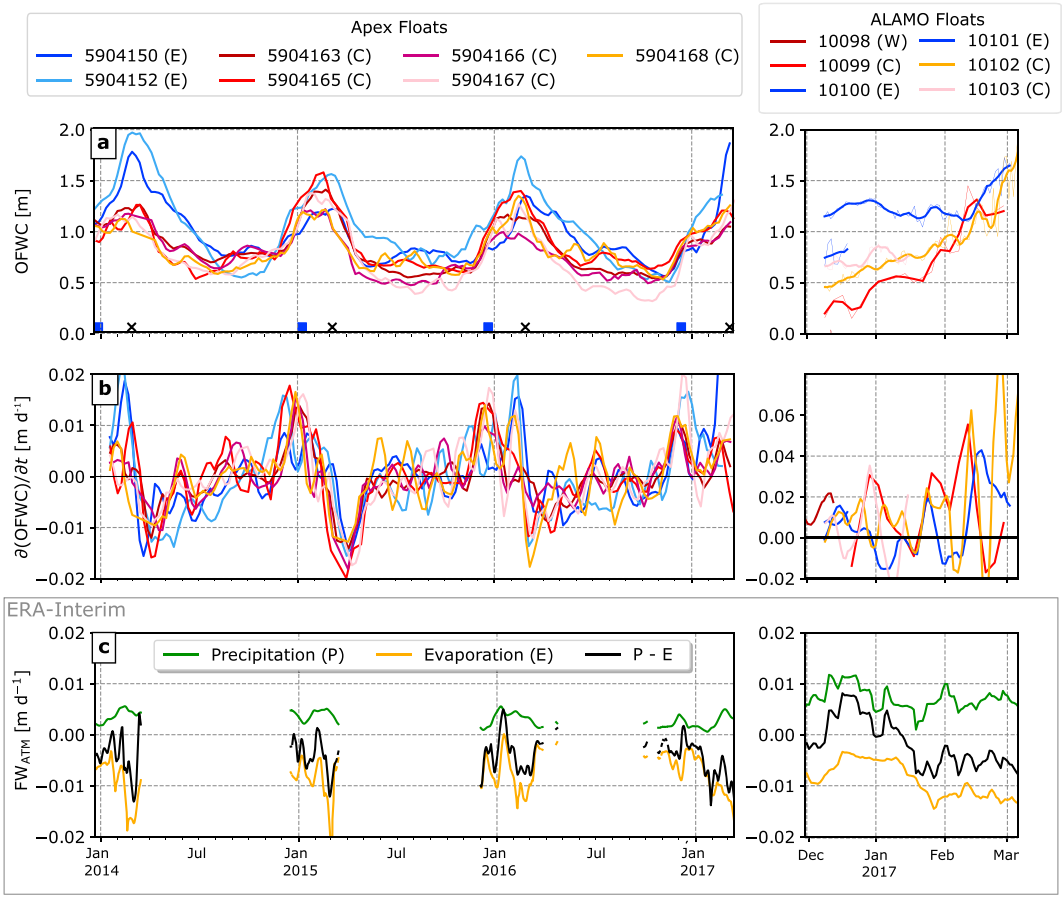

Figure 9. Ocean freshwater content (OFWC) and components of atmospheric moisture flux components. Left plots are for Apex floats; right plots are for ALAMO floats. Rows are from top to bottom: (a) OFWC (m) derived from float measurements, using equation (4). (b) OFWC tendency, d (OFWC)/d*t* (m/day). (c) ERA-Interim estimates of precipitation (P), evaporation (E), and the net atmosphere freshwater surface flux (FW_{ATM}: m/day) for grid cell closest to locations of Apex float 5904163 in the central region, for periods where local satellite-derived sea ice concentration is below 15%. LOWESS smoothing was applied to Apex (30 days) and ALAMO data (14 days); ERA-Interim data are smoothed at 14 days. Note expanded scale for d (OFWC)/d*t* for 2016–2017 ALAMO plot (right). ALAMO = Air-Launched Autonomous Micro Observer.

(Figure 9b) even though local sea ice melt could not be contributing significantly to the observed freshwater flux signal (Figure 5a). The net freshwater gain from the first to last ice-free days for each float for each summer period (Figure 10) was positive, except for one float (Apex 5904168) in 2015. Summer freshwater gains were usually largest in the eastern region. This increase cannot be attributed to local surface freshwater fluxes since sea ice was minimal, and cumulative (*P-E*) from ERA-Interim was negative (Figure 9c and Table 2). The higher values of freshwater gain in summer 2016–2017, relative to earlier summers, may be associated with the same climate anomaly—a strong negative phase of the Southern Annular Mode—responsible for the early loss of sea ice in that year (Turner et al., 2017). The associated wind stress anomaly is directed offshore over the Amundsen Sea (Turner et al., 2017, their Figure 3). This would intensify the westward flow of the Antarctic Coastal Current and drive an increased southward flux of subsurface warm water in the Amundsen Sea to increase the production of freshwater by basal melting of ice shelves (Paolo et al., 2018).

Although surface freshwater fluxes from ERA-Interim have significant uncertainties at high latitudes (Bromwich et al., 2011), we conclude that oceanic freshwater transport must play a significant role in this summertime freshening in the Ross Sea. Previous studies have identified that the westward flow of the Antarctic Coastal Current (Jacobs & Giulivi, 2010; Smith, Sedwick, et al., 2012) brings freshwater from the Amundsen Sea into the eastern Ross Sea, as a combination of liquid freshwater, sea ice, and small

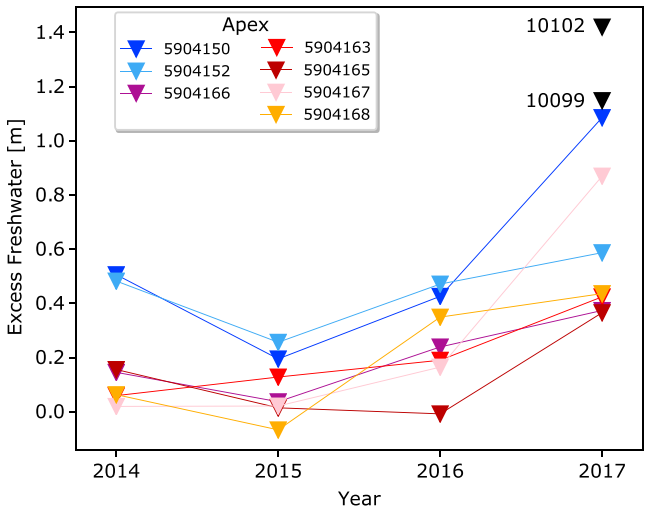

Figure 10. Excess freshwater content, the freshwater content change between the start and end of the ice-free summer season, minus the cumulative (*P-E*) from ERA-Interim over the same period. Apex floats are shown as colored symbols, blues for eastern region floats and red/orange tones for central region floats. For 2017, black symbols indicate values derived from the two Air-Launched Autonomous Micro Observer floats near the Ross Ice Shelf front.

icebergs (Mazur et al., 2017). Moffat et al. (2008) discussed the dynamics of buoyancy-driven coastal currents and their dependence on the seasonal modulation of melt rate. Much of this freshwater input at the Ross Sea's eastern boundary past Cape Colbeck flows along the continental slope in the Antarctic Slope Current (Thompson et al., 2018); however, some turns southward into Little America Basin toward the eastern Ross Ice Shelf front (Orsi & Wiederwohl, 2009, their Figure 5b). Realistic numerical model simulations (Dinniman et al., 2015; Kusahara & Hasumi, 2014; Nakayama et al., 2014) also demonstrate this freshwater pathway. The sources of freshwater in the Amundsen Sea are the rapid melting of its ice shelves (Depoorter et al., 2013; Paolo et al., 2015; Paolo et al., 2018; Pritchard et al., 2012; Rignot et al., 2013) and melting of sea ice in early summer.

We estimated the contribution of lateral advection of freshwater into the eastern Ross Sea using the simulation reported by Nakayama et al. (2014), who showed Amundsen Sea meltwater contributing ~2 m of freshwater to the eastern Ross Sea after 10 years of model integration (their Figure 2b). This contribution suggests an annual-averaged contribution of ~0.2 m/a, which is in the midrange of our observed values of OFWC increases during summer (Figure 10).

The dependence of eastern Ross Sea upper-ocean freshwater and the associated net stratification on upstream ocean/ice processes indicate potential for significant change if the Amundsen Sea continues to experience increased inflows of CDW that drive ice shelf basal melting and modulate the seasonal cycle of sea ice formation and melting (Dinniman et al., 2018; Timmermann & Hellmer, 2013).

4.3. Freshwater Gain Near the Ross Ice Shelf Front During Summer 2016–2017

During summer 2016–2017, ALAMO floats 10099 and 10102 measured increases in OFWC of 1.1 and 1.4 m, respectively (Figure 10), near the Ross Ice Shelf. Following prior studies (e.g., Jacobs & Giulivi, 2010; Nakayama et al., 2014; Smith, Sedwick, et al., 2012) and the analyses in section 4.2, we expect that advection from the Amundsen Sea is a substantial contribution to total freshwater gains near the ice shelf in summer (Smith, Sedwick, et al., 2012).

The freshwater gains observed by these two ALAMO floats are larger than values observed at the Apex floats further north of the ice shelf, suggesting the presence of additional sources of freshwater. Following Jacobs et al. (1985) and Moffat et al. (2008), these potential sources include (i) summer excess ice shelf basal melting under the shallow outer portions of the Ross Ice Shelf (Arzeno et al., 2014; Horgan et al., 2011; Malyarenko et al., 2019; Moholdt et al., 2014), (ii) mass loss from the ice shelf's vertical face (e.g., Gayen et al., 2016; Magorrian & Wells, 2016), and (iii) blowing snow (snow falling on the Ross Ice Shelf that is then blown into open water by the prevailing southerly winds; Knuth et al., 2010).

Table 2
Estimated Freshwater Contribution From Different Sources Near the Ross Ice Shelf Front in the 2016–2017 Summer

Freshwater budget term	Source	Controlling rate[a] and volume	Freshwater (m)[b]
Measured freshwater	ALAMO floats (Figure 10)		0.8–1.4
FW_{ATM}	ERA-Interim	−0.7 mm/day	−0.06
(i) Summer excess ice shelf basal melting	Arzeno et al. (2014)	0.5 m/a over 50 km of ice shelf	0.12
(ii) Mass loss from ice shelf vertical face	Error estimate for InSAR ice velocities	50-m/a loss rate (melting plus small iceberg calving)	0.06
(iii) Blowing snow	ERA-Interim	0.43 m.w.e./a over the northern ice shelf	0.04
Sea ice melt[c]	See section 4.2		0.5[c]

Note. ALAMO = Air-Launched Autonomous Micro Observer.
[a]Mean January/February rates. [b]Meters of freshwater accumulated over 3-month period. [c]For comparison only: freshwater released locally before the start of the sea ice-free summer.

We estimated the magnitudes of these three potential SML freshwater sources for the summer period of about 90 days free of sea ice (Table 2). For both the ice shelf mass loss terms and blowing snow, we assumed that the fluxes at the ice shelf front were distributed evenly over a 50-km-wide zone of open water in front of the ice shelf. For (i), we assume that the summer basal melt rate was ~0.5 m/a higher than the winter mean over a zone of the ice shelf ~50 km wide (Arzeno et al., 2014) and that all summer excess was advected into the open ocean north of the ice shelf front. Over the 90 days of summer, this provided ~0.12 m of freshwater. For (ii), we assume a maximum potential "lateral" melt rate of 50 m/a, corresponding to an error of ~5% in satellite-derived ice shelf velocities of ~1 km/a near the ice shelf front (Mouginot et al., 2012). Our estimate includes formation of small icebergs that might completely melt near the ice shelf front. Assuming a mean ice front thickness of 250 m (Schaffer et al., 2016), this term equates to 0.06 m of freshwater. To estimate (iii), we assumed that all snow falling on the outer 20 km of the Ross Ice Shelf was ultimately blown into the ocean before significant mass loss could occur through evaporation; this estimate is based on satellite visible band images over the Ross Ice Shelf front. A summer precipitation rate on the outer ice shelf of 1.18 mm/day (0.43 m/a) water equivalent applied over 90 days equates to 0.04 m of freshwater averaged over the 50-km open-ocean zone. These three terms (Table 2) sum to roughly 0.2 m of freshwater in excess of that provided by advection.

For comparison, the average summer atmospheric freshwater flux (FW_{ATM}) from ERA-Interim at the central region float locations was −0.7 mm/day (Figure 9c); this is negative because the persistent evaporation from open water (average of ~3.4 mm/day) exceeds the summer precipitation (average of ~2.7 mm/day). The net atmospheric flux integrated over summer was about −0.06 m; this acted against the trend toward freshening during this period.

While each estimate has large uncertainties, this additional freshwater is generally consistent with the elevated OFWC at ALAMOs 10099 and 10102 relative to the easternmost Apex floats (Figure 10). That is, the dominant source of upper-ocean freshwater along the Ross Ice Shelf front in summer is advection from the Amundsen Sea, but additional local sources at the ice shelf significantly increase the freshwater content feeding into the westward flowing current along the ice shelf front.

The excess freshwater along the ice shelf front during summer would increase the upper-ocean buoyancy, improving the efficiency of ventilation of the outer portion of the sub-ice shelf cavity by warmer offshore surface waters (Malyarenko et al., 2019). In turn, this process accelerates ice shelf basal melting. The additional buoyancy also reduces the heat loss required to initiate sea ice formation (Martinson, 1990) in early autumn. The initial stage of sea ice growth near the ice shelf front is not reflected in Special Sensor Microwave Imager time series of C_{ice} because net southerly wind stress drives the freshly formed sea ice away from the front (Figure 1). Increased upper-ocean buoyancy may also suppress deep convection from brine rejection and the resulting production of HSSW in polynyas (Silvano et al., 2018), thus modifying the primary source of ocean heat for melting the grounding lines of deep East Antarctic glaciers flowing into the Ross Ice Shelf (Tinto et al., 2019).

5. Conclusions

Seven Apex (December 2013 to March 2017) and six ALAMO floats (austral summer 2016–2017) have provided the first measurements of seasonal to interannual variability of upper-ocean hydrography over the Ross Sea continental shelf, which is covered by sea ice for about 9 months each year. Setting the parking depths of most floats to deeper than the seabed substantially reduced their lateral motion relative to free drifting floats, allowing the Apex floats to remain on the continental shelf for more than 3 years, sampling four summers. The multiyear records from the Apex float deployments, with weekly profiling, have provided the first accurate measurements of the annual cycle of upper-ocean heat and freshwater content (OHC and OFWC) on the midcontinental shelf. The ALAMO floats obtained profiles with more rapid sampling closer to the Ross Ice Shelf front, providing the first time series of the upper ocean in this region through the development and decay of the summer SML.

The observed increases in OFWC from late winter to the onset of open water conditions are generally consistent with local melting of sea ice, starting at a late winter thickness of ~0.5 m. However, values of OFWC continued to increase after sea ice disappeared, with the largest increases in the eastern Ross Sea and along the Ross Ice Shelf front. This freshening is inconsistent with the modeled excess of evaporation over

precipitation for open water in the Ross Sea in summer. Estimates of the freshwater contributions from the nearby Ross Ice Shelf suggest that it cannot account for all of the excess freshwater, pointing to an advective source of freshwater from further east in the Amundsen Sea. We speculate that the additional freshwater input modifies the ocean stratification and dynamics of water mass exchanges across the ice shelf front, including the subsurface inflow of HSSW, and shallower exchanges of seasonally warmed AASW that leads to relatively high melt rates along the northern Ross Ice Shelf. Additional freshwater also retards the onset of deep convection that produces HSSW in the western Ross Sea in winter.

During the short summer periods during which the Ross Sea was mostly free of sea ice, changes in measured OHC in the upper 120 m of the ocean were substantially smaller (44 ± 18 W/m^2) than those obtained by integrating surface fluxes from the ERA-Interim reanalysis. Some of this difference may be due to errors in the ERA-Interim surface flux that could arise from deficiencies in the radiation budget from a misrepresentation of clouds and the ocean's surface characteristics and the dependence of turbulent fluxes on boundary layer winds and stability. However, as with the freshwater budgets, we propose that one cause of this difference is a flux of cool water (perhaps augmented with low-concentration sea ice and iceberg fragments that melts locally) in the Antarctic Coastal Current which flows westward from the Amundsen Sea. There are no direct measurements of freshwater and heat fluxes into the Ross Sea from the Amundsen Sea, but these fluxes are now represented in high-resolution regional ocean models that include ice shelf melting and sea ice. Future studies of output from these models, guided by the new profiler data sets reported here, should provide new insights into the dependence of hydrographic variability in the Ross Sea on changes in the Amundsen Sea and its rapidly melting ice shelves.

These novel measurements identify the need to improve quantification of freshwater fluxes from the Amundsen Sea to the eastern Ross Sea and along the ice shelf front and to narrow uncertainties in the factors that modulate the atmospheric heat fluxes into the upper ocean in summer. The data set will provide constraints for models of Antarctic SML evolution under a variable sea ice cover, including for the complex region near the Ross Ice Shelf front where offshore katabatic winds modify the sea ice cover and the ocean-atmosphere exchanges of heat, freshwater, and momentum on small spatial and temporal scales. Improved physical understanding of these processes will contribute to other disciplines focused on coastal ecosystems and the response of the Antarctic Ice Sheet to ocean-atmosphere-ice interactions around its margins.

Acknowledgments
This work was supported by the ROSETTA-Ice project funded by NSF Antarctic Integrated System Science, Grants 1443677, 1443498, and 1443534; NSF Ocean Sciences Grant 1357522, and the Gordon and Betty Moore Foundation. Apex floats were supported by the University of Washington NSF Grant OPP-1425989 and NOAA Grant NA150AR4320063. ALAMO floats were procured through the generous support of the Old York Foundation and the Scripps Institution of Oceanography John Dove Isaacs Chair. We thank the New York Air National Guard for their invaluable assistance with ALAMO deployment from their LC-130 aircraft. We are indebted to Stan Jacobs for his insights into Ross Sea oceanography and two thorough, anonymous reviewers of this manuscript. Steve Jayne and colleagues at Woods Hole Oceanographic Institute received and decoded ALAMO data (available at https://www.ldeo.columbia.edu/polar-geophysics-group/publications). Argo data are collected and made freely available by the International Argo Program and the national programs that contribute to it (http://www.argo.ucsd.edu, http://argo.jcommops.org). The Argo Program is part of the Global Ocean Observing System.

References

Ackley, S. F., Xie, H., & Tichenor, E. A. (2015). Ocean heat flux under Antarctic sea ice in the Bellingshausen and Amundsen Seas: Two case studies. *Annals of Glaciology*, *56*(69), 200–210. https://doi.org/10.3189/2015AoG69A890

Argo (2000). Argo float data and metadata from Global Data Assembly Centre (Argo GDAC). SEANOE. http://doi.org/10.17882/42182

Arrigo, K. R., Worthen, D., Schnell, A., & Lizotte, M. P. (1998). Primary production in Southern Ocean waters. *Journal of Geophysical Research*, *103*(C8), 15,587–15,600. https://doi.org/10.1029/98JC00930

Arzeno, I. B., Beardsley, R. C., Limeburner, R., Owens, B., Padman, L., Springer, S. R., et al. (2014). Ocean variability contributing to basal melt rate near the ice front of Ross Ice Shelf, Antarctica. *Journal of Geophysical Research: Oceans*, *119*, 4214–4233. http://doi.org/10.1002/2014JC009792

Bromwich, D. H., Nicolas, J. P., & Monaghan, A. J. (2011). An assessment of precipitation changes over Antarctica and the Southern Ocean since 1989 in contemporary global reanalyses. *Journal of Climate*, *24*(16), 4189–4209. http://doi.org/10.1175/2011JCLI4074.1

Budillon, G., Castagno, P., Aliani, S., Spezie, G., & Padman, L. (2011). Thermohaline variability and Antarctic Bottom Water formation at the Ross Sea shelf break. *Deep Sea Research Part I: Oceanographic Research Papers*, *58*(10), 1002–1018. http://doi.org/10.1016/j.dsr.2011.07.002

CAMLR. (2016), Ross Sea Region Marine Protected Area, Commission for the conservation of Antarctic Marine Living Resources Conservation Measure, 91-05.

Carmack, E., Polyakov, I., Padman, L., Fer, I., Hunke, E., Jackson, J., et al. (2015). Toward quantifying the increasing role of oceanic heat in sea ice loss in the new Arctic. *Bulletin of the American Meteorological Society*, *96*(12), 2079–2105. https://doi.org/10.1175/BAMS-D-13-00177.1

Carmack, E. C. (1986). Circulation and mixing in ice covered waters. In N. Unterstenier (Ed.), *The Geophysics of Sea Ice* (pp. 641–712). New York: Plenum.

Cerovečki, I., Talley, L. D., & Mazloff, M. R. (2011). A comparison of southern ocean air-sea buoyancy flux from an ocean state estimate with five other products. *Journal of Climate*, *24*(24), 6283–6306. http://doi.org/10.1175/2011JCLI3858.1

Charrassin, J.-B., Hindell, M., Rintoul, S. R., Roquet, F., Sokolov, S., Biuw, M., et al. (2008). Southern Ocean frontal structure and sea ice formation rates revealed by elephant seals. *Proceedings of the National Academy of Science*, *105*(33), 11634–11639. https://doi.org/10.1073/pnas.0800790105

Cole, S. T., Timmermans, M.-L., Toole, J. M., Krishfield, R. A., & Thwaites, F. T. (2014). Ekman veering, internal waves, and turbulence observed under Arctic sea ice. *Journal of Physical Oceanography*, *44*(5), 1306–1328. http://doi.org/10.1175/JPO-D-12-0191.1

Comiso, J. C., Kwok, R., Martin, S., & Gordon, A. L. (2011). Variability and trends in sea ice extent and ice production in the Ross Sea. *Journal of Geophysical Research*, *116*, C04021. http://doi.org/10.1029/2010JC006391

Condron, A., Winsor, P., Hill, C., & Menemenlis, D. (2009). Simulated response of the Arctic freshwater budget to extreme NAO wind forcing. *Journal of Climate*, *22*(9), 2422–2437. http://doi.org/10.1175/2008JCLI2626.1

Cox, G. F. N., & Weeks, W. F. (1974). Salinity variations in sea ice. *Journal of Glaciology*, *13*(67), 109–120. http://doi.org/10.3189/S0022143000023418

Dale, E. R., McDonald, A. J., Coggins, J. H. J., & Rack, W. (2017). Atmospheric forcing of sea ice anomalies in the Ross Sea Polynya region. *The Cryosphere*, *11*(1), 1–21. http://doi.org/10.5194/tc-2016-89

DeConto, R. M., & Pollard, D. (2016). Contribution of Antarctica to past and future sea-level rise. *Nature*, *531*(7596), 591–597. http://doi.org/10.1038/nature17145

Dee, D. P., Uppala, S. M., Simmons, A. J., Berrisford, P., Poli, P., Kobayashi, S., et al. (2011). The ERA-Interim reanalysis: Configuration and performance of the data assimilation system. *Quarterly Journal of the Royal Meteorological Society*, *137*(656), 553–597. http://doi.org/10.1002/qj.828

Depoorter, M. A., Bamber, J. L., Griggs, J. A., Lenaerts, J. T. M., Ligtenberg, S. R. M., van den Broeke, M. R., & Moholdt, G. (2013). Calving fluxes and basal melt rates of Antarctic ice shelves. *Nature*, *5*(4), 809–819. https://doi.org/10.5194/tc-5-809-2011

Dinniman, M. S., Klinck, J. M., Bai, L.-S., Bromwich, D. H., Hines, K. M., & Holland, D. M. (2015). The effect of Atmospheric forcing resolution on delivery of ocean heat to the Antarctic floating ice shelves. *Journal of Climate*, *28*(15), 6067–6085. http://doi.org/10.1175/JCLI-D-14-00374.1

Dinniman, M. S., Klinck, J. M., Hofmann, E. E., & Smith, W. O. Jr. (2018). Effects of projected changes in wind, atmospheric temperature, and freshwater inflow on the Ross Sea. *Journal of Climate*, *31*(4), 1619–1635. https://doi.org/10.1175/JCLI-D-17-0351.s1

Fusco, G., Budillon, G., & Spezie, G. (2009). Surface heat fluxes and thermohaline variability in the Ross Sea and in Terra Nova Bay polynya. *Continental Shelf Research*, *29*(15), 1887–1895. https://doi.org/10.1016/j.csr.2009.07.006

Gayen, B., Griffiths, R. W., & Kerr, R. C. (2016). Simulation of convection at a vertical ice face dissolving into saline water. *Journal of Fluid Mechanics*, *798*, 284–298. https://doi.org/10.1017/jfm.2016.315

Gordon, A. L., Huber, B. A., & Busecke, J. (2015). Bottom water export from the western Ross Sea, 2007 through 2010. *Geophysical Research Letters*, *42*, 5387–5394. https://doi.org/10.1002/2015GL064457

Gordon, L., Codispoti, L., Jennings, J., Millero, F., Morrison, J., & Sweeney, C. (2000). Seasonal evolution of hydrographic properties in the Ross Sea, Antarctica, 1996–1997. *Deep Sea Research Part II: Topical Studies in Oceanography*, *47*(15–16), 3095–3117. http://doi.org/10.1016/S0967-0645(00)00060-6

Holland, M. M., Landrum, L., Raphael, M., & Stammerjohn, S. (2017). Springtime winds drive Ross Sea ice variability and change in the following autumn. *Nature Communications*, *8*(1), 731. http://doi.org/10.1038/s41467-017-00820-0

Holland, P. R., & Kwok, R. (2012). Wind-driven trends in Antarctic sea-ice drift. *Nature Geoscience*, *5*(12), 872–875. http://doi.org/10.1038/ngeo1627

Horgan, H. J., Walker, R. T., Anandakrishnan, S., & Alley, R. B. (2011). Surface elevation changes at the front of the Ross Ice Shelf: Implications for basal melting. *Journal of Geophysical Research*, *116*, C02005. http://doi.org/10.1029/2010JC006192

Jackson, J. M., Carmack, E. C., McLaughlin, F. A., Allen, S. E., & Ingram, R. G. (2010). Identification, characterization, and change of the near-surface temperature maximum in the Canada Basin, 1993–2008. *Journal of Geophysical Research*, *115*, C05021. http://doi.org/10.1029/2009JC005265

Jacobs, S. S., & Comiso, J. C. (1989). Sea ice and oceanic processes on the Ross Sea continental shelf. *Journal of Geophysical Research*, *94*(C12), 18,195–18,211. http://doi.org/10.1029/JC094iC12p18195

Jacobs, S. S., Fairbanks, R. G., & Horibe, Y. G. (1985). Origin and evolution of water masses near the Antarctic continental margin: Evidence from H218O/H216O ratios in seawater. In S. S. Jacobs (Ed.), *Oceanology of the Antarctic continental shelf*, *Antarctic Research Series* (pp. 59–85). Washington, DC: American Geophysical Union. http://doi.org/10.1029/AR043

Jacobs, S. S., & Giulivi, C. F. (2010). Large multidecadal salinity trends near the Pacific–Antarctic continental margin. *Journal of Climate*, *23*(17), 4508–4524. http://doi.org/10.1175/2010JCLI3284.1

Joughin, I., Smith, B. E., Shean, D. E., & Floricioiu, D. (2014). Brief communication: Further summer speedup of Jakobshavn Isbræ. *The Cryosphere*, *8*(1), 209–214. http://doi.org/10.5194/tc-8-209-2014

Kim, T. W., Ha, H. K., Wåhlin, A. K., Lee, S., Kim, C. S., Lee, J. H., & Cho, Y. K. (2017). Is Ekman pumping responsible for the seasonal variation of warm circumpolar deep water in the Amundsen Sea? *Continental Shelf Research*, *132*, 38–48. https://doi.org/10.1016/j.csr.2016.09.005

Klatt, O., Boebel, O., & Fahrbach, E. (2007). A profiling float's sense of ice. *Journal of Atmospheric and Oceanic Technology*, *24*(7), 1301–1308. https://doi.org/10.1175/JTECH2026.1

Knuth, S. L., Tripoli, G. J., Thom, J. E., & Weidner, G. A. (2010). The influence of blowing snow and precipitation on snow depth change across the Ross Ice Shelf and Ross Sea regions of Antarctica. *Journal of Applied Meteorology and Climatology*, *49*(6), 1306–1321. https://doi.org/10.1175/2010JAMC2245.1

Kurtz, N. T., & Markus, T. (2012). Satellite observations of Antarctic sea ice thickness and volume. *Journal of Geophysical Research*, *117*, C08025. http://doi.org/10.1029/2012JC008141

Kusahara, K., & Hasumi, H. (2014). Pathways of basal meltwater from Antarctic ice shelves: A model study. *Journal of Geophysical Research: Oceans*, *119*, 5690–5704. http://doi.org/10.1002/2014JC009915

Ledwell, J. R., Watson, A. J., & Law, C. S. (1993). Evidence for slow mixing across the pycnocline from an open-ocean tracer-release experiment. *Nature*, *364*(6439), 701–703. https://doi.org/10.1038/364701a0

Lenaerts, J. T. M., Van Tricht, K., Lhermitte, S., & L'Ecuyer, T. S. (2017). Polar clouds and radiation in satellite observations, reanalyses, and climate models. *Geophysical Research Letters*, *44*, 3355–3364. http://doi.org/10.1002/2016GL072242

Li, Y., McGillicuddy, D. J., Dinniman, M. S., & Klinck, J. M. (2017). Processes influencing formation of low-salinity high-biomass lenses near the edge of the Ross Ice Shelf. *Journal of Marine Systems*, *166*, 108–119. http://doi.org/10.1016/j.jmarsys.2016.07.002

Little, C. M., & Urban, N. M. (2016). CMIP5 temperature biases and 21st century warming around the Antarctic coast. *Annals of Glaciology*, *57*(73), 69–78. http://doi.org/10.1017/aog.2016.25

Locarnini, R. A., Mishonov, A. V., Antonov, J. I., Boyer, T. P., Garcia, H. E., Baranova, O. K., et al. (2013). World Ocean Atlas 2013 Volume 1: Temperature. In S. Levitus & A. Mishonov (Eds.), *NOAA Atlas NESDIS* (Vol. *73*, 1–40). Washington DC: US Gov. Printing Office.

MacAyeal, D. R., & Thomas, R. H. (1986). The effects of basal melting on the present flow of the Ross Ice Shelf, Antarctica. *Journal of Glaciology*, *32*(110), 72–86. https://doi.org/10.1017/S0022143000006900

Magorrian, S. J., & Wells, A. J. (2016). Turbulent plumes from a glacier terminus melting in a stratified ocean. *Journal of Geophysical Research: Oceans*, *121*, 4670–4696. https://doi.org/10.1002/2015JC011160

Malyarenko, A., Robinson, N. J., Williams, M. J. M., & Langhorne, P. J. (2019). A wedge mechanism for summer surface water in flow into the Ross ice shelf cavity. *Journal of Geophysical Research: Oceans*, *124*, 1196–1214. https://doi.org/10.1029/2018JC014594

Markus, T., & Cavalieri, D. J. (2000). An enhancement of the NASA Team sea ice algorithm. *IEEE Transactions on Geoscience and Remote Sensing*, *38*(3), 1387–1398. http://doi.org/10.1109/36.843033

Martin, S., Drucker, R., & Kwok, R. (2007). The areas and ice production of the western and central Ross Sea polynyas, 1992–2002, and their relation to the B-15 and C-19 iceberg events of 2000 and 2002. *Journal of Marine Systems*, *68*(1–2), 201–214. http://doi.org/10.1016/j.jmarsys.2006.11.008

Martinson, D. G. (1990). Evolution of the Southern Ocean winter mixed layer and sea ice: Open ocean deepwater formation and ventilation. *Journal of Geophysical Research*, *95*(C7), 11,641–11,654. http://doi.org/10.1029/JC095iC07p11641

Martinson, D. G., & McKee, D. C. (2012). Transport of warm upper circumpolar deep water onto the Western Antarctic Peninsula Continental Shelf. *Ocean Science*, *8*(4), 433–442. http://doi.org/10.5194/os-8-433-2012

Mazur, A. K., Wåhlin, A. K., & Krężel, A. (2017). An object-based SAR image iceberg detection algorithm applied to the Amundsen Sea. *Remote Sensing of Environment*, *189*, 67–83. http://doi.org/10.1016/j.rse.2016.11.013

Moffat, C., Beardsley, R. C., Owens, B., & van Lipzig, N. (2008). A first description of the Antarctic Peninsula Coastal Current. *Deep Sea Research Part II: Topical Studies in Oceanography*, *55*(3–4), 277–293. http://doi.org/10.1016/j.dsr2.2007.10.003

Moholdt, G., Padman, L., & Fricker, H. A. (2014). Basal mass budget of Ross and Filchner-Ronne ice shelves, Antarctica, derived from Lagrangian analysis of ICESat altimetry. *Journal of Geophysical Research: Earth Surface*, *119*, 2361–2380. http://doi.org/10.1002/2014JF003171

Mouginot, J., Scheuchl, B., & Rignot, E. (2012). Mapping of ice motion in Antarctica using synthetic-aperture radar data. *Remote Sensing*, *4*(9), 2753–2767. https://doi.org/10.3390/rs4092753

Nakayama, Y., Timmermann, R., Rodehacke, C. B., Schröder, M., & Hellmer, H. H. (2014). Modeling the spreading of glacial meltwater from the Amundsen and Bellingshausen Seas. *Geophysical Research Letters*, *41*, 7942–7949. http://doi.org/10.1002/2014GL061600

Nelson, M. J. S., Queste, B. Y., Smith, I. J., Leonard, G. H., Webber, B. G. M., & Hughes, K. G. (2017). Measurements of ice shelf water beneath the front of the Ross Ice Shelf using gliders. *Annals of Glaciology*, *58*(74), 41–50. http://doi.org/10.1017/aog.2017.34

Orsi, A. H., Johnson, G. C., & Bullister, J. L. (1999). Circulation, mixing, and production of Antarctic Bottom Water. *Progress in Oceanography*, *43*(1), 55–109. https://doi.org/10.1016/S0079-6611(99)00004-X

Orsi, A. H., & Wiederwohl, C. L. (2009). A recount of Ross Sea waters. *Deep Sea Research Part II: Topical Studies in Oceanography*, *56*(13–14), 778–795. http://doi.org/10.1016/j.dsr2.2008.10.033

Padman, L., Costa, D. P., Dinniman, M. S., Fricker, H. a., Goebel, M. E., Huckstadt, L. A., et al. (2012). Oceanic controls on the mass balance of Wilkins Ice Shelf, Antarctica. *Journal of Geophysical Research*, *117*, C01010. http://doi.org/10.1029/2011JC007301

Paolo, F. S., Fricker, H. A., & Padman, L. (2015). Volume loss from Antarctic ice shelves is accelerating. *Science*, *348*(6232), 327–331. http://doi.org/10.1126/science.aaa0940

Paolo, F. S., Padman, L., Fricker, H. A., Adusumilli, S., Howard, S., & Siegfried, M. R. (2018). Response of Pacific-sector Antarctic ice shelves to the El Niño/Southern Oscillation. *Nature Geoscience*, *11*(2), 121–126. https://doi.org/10.1038/s41561-017-0033-0

Pellichero, V., Sallée, J.-B., Schmidtko, S., Roquet, F., & Charrassin, J.-B. (2017). The ocean mixed layer under Southern Ocean sea-ice: Seasonal cycle and forcing. *Journal of Geophysical Research: Oceans*, *122*, 1608–1633. http://doi.org/10.1002/2016JC011970

Petty, A. A., Feltham, D. L., & Holland, P. R. (2013). Impact of atmospheric forcing on Antarctic continental shelf water masses. *Journal of Physical Oceanography*, *43*(5), 920–940. http://doi.org/10.1175/JPO-D-12-0172.1

Petty, A. A., Holland, P. R., & Feltham, D. L. (2014). Sea ice and the ocean mixed layer over the Antarctic shelf seas. *The Cryosphere*, *8*(2), 761–783. http://doi.org/10.5194/tc-8-761-2014

Pillsbury, R. D., & Jacobs, S. S. (1985). Preliminary observations from long-term current meter moorings near the Ross Ice Shelf, Antarctica. In *Oceanology of the Antarctic Continental Shelf*, *Antarctic Research Series* (Vol. 43, pp. 87–107). Washington, D.C: American Geohysical Union. http://doi.org/10.1029/AR043p0087

Piñones, A., Hofmann, E. E., Costa, D. P., Goetz, K., Burns, J. M., Roquet, F., et al. (2019). Hydrographic variability along the inner and mid-shelf region of the western Ross Sea obtained using instrumented seals. *Progress in Oceanography*, in press, *174*, 131–142. http://doi.org/10.1016/j.pocean.2019.01.003

Pritchard, H., Ligtenberg, S. R. M., Fricker, H. A., Vaughan, D. G., Van den Broeke, M. R., & Padman, L. (2012). Antarctic ice-sheet loss driven by basal melting of ice shelves. *Nature*, *484*(7395), 502–505. https://doi.org/10.1038/nature10968

Rignot, E., Jacobs, S., Mouginot, J., & Scheuchl, B. (2013). Ice-shelf melting around Antarctica. *Science*, *341*(6143), 266–270. http://doi.org/10.1126/science.1235798

Riser, S. C., Freeland, H. J., Roemmich, D., Wijffels, S., Troisi, A., Belbéoch, M., et al. (2016). Fifteen years of ocean observations with the global Argo array. *Nature Climate Change*, *6*(2), 145–153. https://doi.org/10.1175/JCLI-D-12-00834.1

Robinson, N. J., Williams, M. J. M., Barrett, P. J., & Pyne, A. R. (2010). Observations of flow and ice-ocean interaction beneath the McMurdo Ice Shelf, Antarctica. *Journal of Geophysical Research*, *115*, C03025. http://doi.org/10.1029/2008JC005255

Rodrigo, J. S., Buchlin, J.-M., van Beeck, J., Lenaerts, J. T. M., & van den Broeke, M. R. (2013). Evaluation of the Antarctic surface wind climate from ERA reanalyses and RACMO2/ANT simulations based on automatic weather stations. *Climate Dynamics*, *40*(1-2), 353–376. http://doi.org/10.1007/s00382-012-1396-y

Roemmich, D., Johnson, G., Riser, S., Davis, R., Gilson, J., Owens, W. B., et al. (2009). The Argo Program: Observing the global oceans with profiling floats. *Oceanography*, *22*(2), 34–43. http://doi.org/10.5670/oceanog.2009.36

Roquet, F., Wunsch, C., & Forget, G. (2013). Estimates of the Southern Ocean general circulation improved by animal-borne instruments. *Geophysical Research Letters*, *40*, 6176–6180. http://doi.org/10.1002/2013GL058304

Rusciano, E., Budillon, G., Fusco, G., & Spezie, G. (2013). Evidence of atmosphere–sea ice–ocean coupling in the Terra Nova Bay polynya (Ross Sea—Antarctica). *Continental Shelf Research*, *61-62*, 112–124. http://doi.org/10.1016/j.csr.2013.04.002

Scambos, T. A., Haran, T. M., Fahnestock, M. A., Painter, T. H., & Bohlander, J. (2007). MODIS-based Mosaic of Antarctica (MOA) data sets: Continent-wide surface morphology and snow grain size. *Remote Sensing of Environment*, *111*(2-3), 242–257. https://doi.org/10.1016/j.rse.2006.12.020

Schaffer, J., Timmermann, R., Arndt, J. E., Kristensen, S. S., Mayer, C., Morlighem, M., & Steinhage, D. (2016). A global high-resolution data set of ice sheet topography, cavity geometry and ocean bathymetry. *Earth System Science Data*, *8*(2), 543–557. http://doi.org/10.5194/essd-8-543-2016

Schmidtko, S., Heywood, K. J., Thompson, A. F., & Aoki, S. (2014). Multidecadal warming of Antarctic waters. *Science*, *346*(6214), 1227–1231. https://doi.org/10.1126/science.1256117

Shepherd, A., Fricker, H. A., & Farrell, S. L. (2018). Trends and connections across the Antarctic cryosphere. *Nature*, *558*(7709), 223–232. https://doi.org/10.1038/s41586-018-0171-6

Silvano, A., Rintoul, S. R., Kusahara, K., Peña-Molino, B., van Wijk, E, Gwyther, D. E., Williams, G. D. (2019). Seasonality of warm water intrusions onto the continental shelf near the Totten Glacier. *Journal of Geophysical Research: Oceans*, *124*. https://doi.org/10.1029/2018JC014634

Silvano, A., Rintoul, S. R., Peña-Molino, B., Hobbs, W. R., van Wijk, E., Aoki, S., et al. (2018). Freshening by glacial meltwater enhances melting of ice shelves and reduces formation of Antarctic Bottom Water. *Science Advances*, *4*(4), eaap9467. http://doi.org/10.1126/sciadv.aap9467

Smethie, W. M., & Jacobs, S. S. (2005). Circulation and melting under the Ross Ice Shelf: Estimates from evolving CFC, salinity and temperature fields in the Ross Sea. *Deep Sea Research Part I: Oceanographic Research Papers*, *52*(6), 959–978. http://doi.org/10.1016/j.dsr.2004.11.016

Smith, D. A., & Klinck, J. M. (2002). Water properties on the west Antarctic Peninsula continental shelf: A model study of effects of surface fluxes and sea ice. *Deep Sea Research Part II: Topical Studies in Oceanography*, *49*(21), 4863–4886. http://doi.org/10.1016/S0967-0645(02)00163-7

Smith, W., Sedwick, P., Arrigo, K., Ainley, D., & Orsi, A. (2012). The Ross Sea in a sea of change. *Oceanography*, *25*(3), 90–103. http://doi.org/10.5670/oceanog.2012.80

Smith, W. O. Jr., Ainley, D. G., Cattaneo-Vietti, R., & Hofmann, E. E. (2012). The Ross Sea continental shelf: Regional biogeochemical cycles, trophic interactions, and potential future changes. In *Antarctic ecosystems: an extreme environment in a changing world* (Vol. 46, pp. 213–242). Chichester, UK: John Wiley & Sons, Ltd. https://doi.org/10.1002/9781444347241.ch7

Stewart, C. L., Christoffersen, P., Nicholls, K. W., Williams, M. J., & Dowdeswell, J. A. (2019). Basal melting of Ross Ice Shelf from solar heat absorption in an ice-front polynya. *Nature Geoscience*, *12*(6), 435–440. https://doi.org/10.1038/s41561-019-0356-0

Thompson, A. F., Stewart, A. L., Spence, P., & Heywood, K. J. (2018). The Antarctic slope current in a changing climate. *Reviews of Geophysics*, *56*, 741–770. https://doi.org/10.1029/2018RG000624

Timmermann, R., & Hellmer, H. H. (2013). Southern Ocean warming and increased ice shelf basal melting in the twenty-first and twenty-second centuries based on coupled ice-ocean finite-element modelling. *Ocean Dynamics*, *63*(9–10), 1011–1026. http://doi.org/10.1007/s10236-013-0642-0

Tinto, K. J., Padman, L., Siddoway, C. S., Springer, S. R., Fricker, H. A., Das, I., et al. (2019). Ross Ice Shelf response to climate driven by the tectonic imprint on seafloor bathymetry. *Nature Geoscience*, *12*(6), 441–449. https://doi.org/10.1038/s41561-019-0370-2

Tschudi, M., Fowler, C., Maslanik, J., Stewart, J. S., & Meier, W. (2016). *Polar Pathfinder daily 25 km EASE-Grid Sea Ice Motion Vectors, Version 3*. Boulder, Colorado USA: NASA National Snow and Ice Data Center Distributed Active Archive Center. https://doi.org/10.5067/O57VAIT2AYYY

Turner, J., Phillips, T., Marshall, G. J., Hosking, J. S., Pope, J. O., Bracegirdle, T. J., & Deb, P. (2017). Unprecedented springtime retreat of Antarctic sea ice in 2016. *Geophysical Research Letters*, *44*, 6868–6875. http://doi.org/10.1002/2017GL073656

Whitworth, T., & Orsi, A. H. (2006). Antarctic Bottom Water production and export by tides in the Ross Sea. *Geophysical Research Letters*, *33*, L12609. http://doi.org/10.1029/2006GL026357

Wong, A. P. S., & Riser, S. C. (2011). Profiling float observations of the upper ocean under sea ice off the Wilkes Land Coast of Antarctica. *Journal of Physical Oceanography*, *41*(6), 1102–1115. http://doi.org/10.1175/2011JPO4516.1